Exploring entanglement phenomena with near-term quantum computers

UNIVERSITY OF TURKU
Department of Physics and Astronomy

Anton Nykänen Exploring entanglement phenomena with near-term quantum computers

Master's thesis, 73 pp.
Theoretical Physics
July 2021

A methodology to explore quantum entanglement phenomena on near-term quantum computers is presented. The method combines two prominent Noisy Intermediate-Scale Quantum (NISQ) algorithms, the variational quantum eigensolver (VQE) and pairwise tomography, to extract pairwise quantum properties from quantum many-body systems. VQE prepares a parametrized quantum circuit and optimizes it to represent the ground state of the system under study. Pairwise tomography provides an exponential decrease in the required measurements to construct two-qubit reduced density matrices.

Two pairwise quantities, mutual information and concurrence, are used to construct complex network representations of the system. Then, network properties can be used to analyze the entanglement structures. Three quantum spin chains are explored: the Ising model, the spin-1/2 XX model and the XXZ model. The methodology is benchmarked with known results and new results for the XXZ model are presented.

Applications for the study of fundamental physics are explored. More specifically, emergent space from quantum entanglement is studied. Mutual information between parts of a redundancy-constrained system is used to define a metric that is then embedded into a smooth manifold embedded in $\mathbb{R}^D$. Effects of entanglement perturbations on the geometry of the embedding are studied.

Keywords: quantum computing, quantum computer, variational quantum eigensolver, VQE, pairwise tomography, NISQ, entanglement, emergent space, complex networks, quantum simulation

UNIVERSITY OF TURKU
Fysiikan ja tähtitieteen laitos

Anton Nykänen Kvanttilomittumisilmiöiden tutkiminen lähitulevaisuuden kvanttitietokoneilla

Pro Gradu, 73 pp.
Teoreettinen fysiikka
Heinäkuu 2021

Tässä Pro Gradussa esitetään metodologia, jonka avulla voidaan tutkia kvanttilomittumisilmiöitä lähitulevaisuuden kvanttitietokoneilla. Tämä metodi yhdistää kaksi merkittävää kvanttialgoritmia, jotka ovat Variaationaalinen KvanttiOminaisarvoLaskija (VKOL) (eng. Variational Quantum Eigensolver (VQE)) ja parittainen kvanttitilatomografia (eng. pairwise quantum state tomography). Nämä algoritmit on suunniteltu lähitulevaisuuden meluisille keskikokoisille kvattitietokoneille (MEKEKVA (eng. noisy intermediate-scale quantum (NISQ)) sopiviksi. VKOL valmistaa parametrisoidun kvanttipiirin, jonka se optimoi edustamaan tutkittavana olevan systeemin perustilaa. Parittainen kvanttitilatomografia laskee exponentiaalisesti tarvittavien mittausten määrää, jotta systeemin perustilasta saadaan rakennettua redusoidut tiheysmatriisit kaikille kahden kubitin pareille. Näistä redusoiduista tiheysmatriiseista voidaan laskea parittaisia ominaisuuksia systeemin perustilalle.

Kahta parittaista ominaisuutta, yhteistä informaatiota (eng. mutual information) ja konkurrensia (eng. concurrence), käytetään muodostamaan systeemille kompleksiset verkostoesitykset. Näiden verkostojen ominaisuuksilla voidaan sitten analysoida kvanttilomittumisrakenteita. Kolmea kvanttispiniketjua tutkitaan: Ising mallia, spin-1/2 XX mallia sekä XXZ mallia. Tässä tutkielmassa esitetyn metodin suorituskykyä testataan vertaamalla saatuja tuloksia jo tunnettuihin tuloksiin. Sen lisäksi, myös uusia tuloksia esitetään XXZ mallille.

Metodin käyttökohteita fundamentaalisen fysiikan tutkimuksessa tutkitaan myös. Tutkimuksen kohteena on emergentin avaruuden syntyminen kvanttilomittumisesta. Redundanssirajoitettujen (eng. redundancy-constrained) systeemien välistä yhteistä informaatiota käytetään luomaan metriikka, joka upotetaan sileään monistoon, joka on upotettuna $\mathbb{R}^D$:hen. Kvanttilomittumisen häiriöiden vaikutusta upotuksen geometriaan tutkitaan.

Avainsanat: kvanttitietokone, kvanttilaskenta, variaationaalinen kvanttiominaisarvolaskija, parittainen kvanttitilatomografia, kvanttilomittuminen, emergentti avaruus, kompleksiset verkostot, kvanttisimulaatio

Contents

Introduction

In the age of developing quantum technology, advances in hardware and algorithms are both important. However, hardware is usually the limiting factor and algorithms have to be designed while keeping the limitations of hardware in mind. Through clever design much can still be achieved and, in this thesis, I will introduce a new method that combines existing algorithms in order to study quantum entanglement phenomena in many-body systems efficiently.

A quantum mechanical model of Turing machine was proposed by Paul Benioff in 1980 [1] but the idea to simulate systems that classical computers could not by using quantum computers came from Yuri Manin and Richard Feynman in 1981 [2], [3]. The field did not kick off until Peter Shor developed an algorithm for integer factorization, a threat to RSA-encryption, which would beat even the best classical computers at the task [4].

Unfortunately, we are still far away from utilizing Shor's algorithm and many other similar algorithms that are designed to be used with large amounts of fault-tolerant (error free) quantum bits, qubits. The advantages brought by the quantum mechanical properties of quantum bits are easily destroyed by noise and environmental effects.

In the near term era we are forced to rely on Noisy Intermediate-Scale Quantum (NISQ) devices and algorithms designed specifically to bypass the limitations of the current state of the art quantum technologies [5]. The development of these algorithms has been swift and we are nearing the point when we achieve quantum supremacy on a problem with real-life consequences. It is likely that in the next five years some NISQ algorithm will be used in drug or chemical development [6, 7].

Meanwhile, the same algorithms can be used for fundamental research of physics. Development in quantum information and the theory of quantum many-body systems is also in acceleration. A recent approach is the study of emergent phenomena

that cannot be described by laws of reduced parts of the system but instead need a holistic view of the whole system. Interesting examples are network entanglement structures in quantum many-body systems and space emerging from quantum entanglement both of which will be studied in this thesis [8, 9].

The goal of this thesis is to introduce a method that one can use for research of various different quantum entanglement phenomena. The study of these phenomena quickly becomes classically intractable as the systems size grows beyond trivial problems. Also, classical simulations are restricted to problems with low amount of entanglement. Here, the method is proven to work with examples of systems with small number of qubits. The method is scalable and as the development of quantum hardware proceeds, it can be used with systems of arbitrary sizes and amounts of entanglement.

The method consists mainly of two parts: a Variational Quantum Eigensolver (VQE), which is used to find the ground state of the system under investigation, and pairwise tomography, which can efficiently extract pairwise quantum information from this ground state [10, 11]. Both algorithms have been recently developed and their efficiency can still be improved. Although many advanced versions exist for VQE, only the simplest version of it will be considered here.

The structure of this thesis is the following. The first chapter will introduce the tools that are needed to construct the whole method. Quantum computing will be introduced followed by VQE and pairwise tomography. In the second part of this thesis, this method is then used, as a proof of concept, first to explore network entanglement structures of quantum many-body systems and then to study quantum gravity and space emerging from entanglement.

1 Quantum computing now and in the near future

We live in the age of information technology where mobile phones, computers and other electric devices all work on the principle of a binary computation system, bits. Even though technology keeps advancing and faster computers with more computing power are built, they all are still just physical representations of the same computation model called Turing Machine. Being essentially the same model, they all share the same limitations and the classes of problems they can calculate. On the other hand, in the world of physics, we are exploring this new frontier of quantum information and quantum entanglement. A great question then arises: are quantum systems computable with the Turing Machine model? We know that some systems are, but generally the answer is not yet known. The general consensus though is that all systems are not and the essence of this is captured in the quote from Richard Feynman in 1981: "Nature isn't classical, dammit, and if you want to make a simulation of nature, you'd better make it quantum mechanical, and by golly it's a wonderful problem, because it doesn't look so easy. "[3] And so the idea of quantum computing was born.

Instead of bits, as in classical computers, we now have quantum bits as our fundamental information-carrying components [5]. These quantum bits, which are also called qubits, are abstract mathematical objects that can be realised in various physical settings. The most common and also promising technology is superconducting circuits, which are cooled down to near absolute zero to minimize environment interaction. This technology is used by IBM in their quantum computing platform IBM Quantum Experience, which is available as a cloud service and is used throughout this thesis. Other possible technologies for quantum computers are based on quantum optics and trapped ions.

1.1   The model of quantum computing

Quantum computing is based upon manipulation of quantum bits, qubits. A qubit lives in 2 dimensional Hilbert space where the basis vectors in Z-base are generally denoted $|0\rangle$ and $|1\rangle$. These can be used analogously to classical bits for computation but the quantum advantage of this model lies in states that are in superposition. A superposition of these basis states is just a linear combination of them

$$|\psi\rangle = \alpha|0\rangle + \beta|1\rangle \tag{1}$$

where α and β are called amplitudes of the corresponding basis states. The state can also be presented in vector notation as $\binom{\alpha}{\beta}$. A qubit stays in superposition until measurement if not disturbed and then the probability to measure $|0\rangle$ is given by the Born rule $P(|0\rangle) = |\langle 0|\psi\rangle|^2 = |\alpha|^2$ and similarly $P(|1\rangle) = |\langle 1|\psi\rangle|^2 = |\beta|^2$. A superposition of states allows for computational advantage with parallel computation. However, the measurement process in the end results in only one measurement result and the superposition state is destroyed in the process. Therefore, all the information encoded in the superposition of the state is not available at once and clever manipulation of the interference is required to obtain computational advantage.

The other quantum resource, in addition to superposition, is quantum entanglement. Entanglement means correlation between states on a quantum level which is quite different from classical correlation. Imagine a book with 100 pages. If the book were classical, you would learn 1% of its contents by reading one page. If the book instead were quantum with information spread in the entanglement between all the pages, you would learn nothing by reading just one page. To obtain information from this quantum book you would need to observe the contents of many pages at once [5]. An example of an entangled state is

$$|\Psi\rangle = \frac{1}{\sqrt{2}}(|00\rangle + |11\rangle). \tag{2}$$

Notation $|00\rangle$ is a shorthand for the tensor product of two qubits $|0\rangle \otimes |0\rangle = |0\rangle|0\rangle =$

$|00\rangle$, which is a state with Hilbert space of $2^N = 2^2 = 4$ dimensions, where N is the number of qubits. The state (2) is entangled in such a way that if qubit one is measured we know immediately the state of the second qubit to be the same as the measurement value of the first, and vice versa.

The amount of entanglement is usually the key aspect determining whether a quantum state can be simulated on a classical computer or not. Simulating a quantum system requires storing the information of its quantum state into a memory and then using it in calculations, e.g., how the state evolves in time. In a highly entangled state, the amount of amplitudes that one needs to store increases as 2^N, so a system of just a few hundred qubits would require more bits than there are atoms in the observable universe [5]. Therefore highly entangled systems with nontrivial amount of qubits can not be simulated efficiently with classical computers. For systems with low entanglement there exist many techniques to approximately simulate them such as Tensor Networks using Matrix Product States (MPS)[12].

The state of the system does not provide all the interesting information. If one wants to know the energy of the system and how it evolves in time then more is needed. The Hamiltonian of a given system encodes all this critical information. In addition to characterising physical systems, other problems can also be encoded into a Hamiltonian form such as optimisation problems. [13]

There are broadly two ways in which a quantum computer can be used. The first one is the simulation of quantum systems which can also be divided into analog and digital quantum simulation. In analog quantum simulation the problem Hamiltonian is mapped to the Hamiltonian of the system performing the computation. The problem is then run on the quantum simulator and the result is mapped back to the original problem. This method is limited by the class of system Hamiltonians that are possible to be simulated on a given analog simulator. Instead, digital quantum simulators can simulate any physical systems regardless of its Hamiltonians. The

problem is mapped to the discrete building blocks of the quantum simulator such as quantum gates in the quantum circuit model. [13]

The other use of quantum computers is different algorithms. The two well-known examples are Shor's algorithm for integer factorization and Grover's algorithm for database searching. These belong to computation complexity class Bounded-error Quantum Polynomial-time (BQP) for which there does not yet exist efficient classical algorithms and therefore these algorithms offer speed-ups compared to their classical counterparts. The speed-up with Grover's algorithm is just quadratic, but with Shor's algorithm, one can get exponential speed up, which is why it is often introduced when discussing possible quantum computing advantages. However, these algorithms are not yet actually usable for interesting problem sizes because they need large amounts of fault-tolerant qubits. A fault-tolerant qubit is free from all noise coming from environment and errors occurring during computation, which is not achievable with current state-of-the-art technology. Methods to counter qubit errors exist, called quantum error correction codes, but they all rely in huge overheads of physical qubits. For context, factorisation of a 2084 bit integer with Shor's algorithm using a planar quantum error correction code would take 8 hours and use 20 million noisy qubits [14]. The current state-of-the-art quantum computer is 65 noisy qubits [15].

1.1.1 NISQ era

Constructing a qubit with desired properties is challenging. The qubits need to be sufficiently protected from environment to preserve the quantum information. At the same time, the qubits are required to strongly interact with other qubits in order for us to perform quantum computation with them. We need to be able to control the qubits and, in the end, measure them. Different physical approaches are better at dealing with these requirements than others, but it is hard to satisfy all of them.

In the far future, all these can most likely be achieved, but in the near future, we have to make the best of what we have available. [5]

This near term quantum computing era is described by the term coined by John Preskill: *NISQ*, which stands for *Noisy Intermediate-Scale Quantum.* In this era, we will have access only to quantum computers with numbers of qubits ranging from 50 to few hundred. 50 qubits itself is a significant milestone because an entangled quantum system with 2^{50} amplitudes is more than the most powerful existing supercomputers can store and compute. However, the qubits are noisy, which greatly limits the power of these quantum computers. The error rate per two-qubit gates in best superconducting circuit hardware is above 0.1% [16]. This limits the length of computable quantum circuits around 1000 gates, as the noise accumulates in longer circuits and overwhelms the signal making the quantum information unreadable. The execution time of these gates also matters and long computation times also lead to decoherence of results. Finally, the physical layout of the qubits also affect how the qubits can interact with each other. Keeping these in mind we can design algorithms suitable for current quantum devices. [5]

1.1.2 Circuit model of quantum computation

Before discussing NISQ algorithms, I will first explain the general circuit model of quantum computation. Other models such as adiabatic quantum computing and one-way quantum computing exist, but the circuit model is the most widely used and it is the one used by IBM's quantum computers. The quantum circuit model is somewhat analogous to classical electrical circuits, as it consists of wires and logical gates. An example circuit is shown in Figure 1. The computation according to the circuit diagram advances from left to right. Each line represents a qubit and its evolution, and the elements on the line are the logical actions applied on the qubit. The line is not a physical wire, but can instead describe the passage of time or the
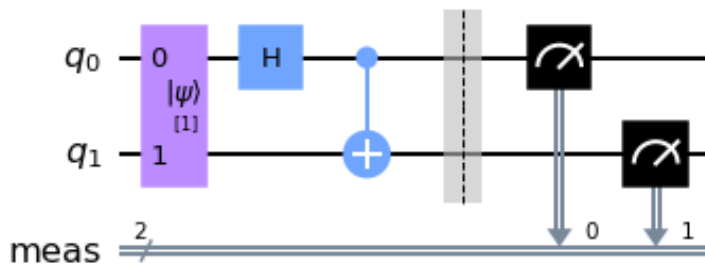
Figure 1: An example of a quantum circuit that creates one of the Bell states and measures it. First, the qubits are initialized in the $|01\rangle$ state. Then, a sequence of quantum gates are applied and the state becomes $\frac{1}{2}(|00\rangle - |11\rangle)$. The dashed line is just a barrier for visualization purposes. In the end, both qubits are measured, and the results are stored into classical bits. [18]

movement of a particle through space. A quantum computation in the circuit model begins with the initialization of the qubits, followed by an arbitrary amount of gates applied to the qubits, and the qubits are finally measured. [17]

The quantum circuit is first initialized to some initial state. Generally it is initialized in the computational basis state as the state consisting of all $|0\rangle$s. So, for a system of N qubits, the initial state is the product state $|0\rangle^{\otimes N} = |0\rangle \otimes \ldots \otimes |0\rangle$. $\underset{N \text{ times}}{}$ Other initial states can be prepared by using quantum gates. Another common initial state is the state $|+\rangle^{\otimes N}$, where the state of one qubit $|+\rangle = \frac{1}{\sqrt{2}}(|0\rangle + |1\rangle)$ is a balanced superposition of the computational Z-basis. In the X-basis, states $|+\rangle$ and $|-\rangle$ form the basis set, where $|-\rangle = \frac{1}{\sqrt{2}}(|0\rangle - |1\rangle)$. [17]

After the initialization, the state is then modified by different quantum gates. The set of gates that are physically available depend on the physical quantum computer in use and they are commonly one-qubit and two-qubit gates, i.e., they act on one qubit and two qubits at a time, respectively. However, we can perform any arbitrary unitary quantum operation if the available set of gates is universal [17]. A
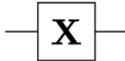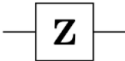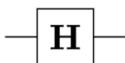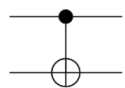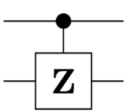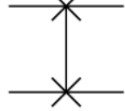
Operator	Gate	Matrix
Pauli-X (X)	$\boxed{X}$	$\begin{bmatrix} 0 & 1 \\ 1 & 0 \end{bmatrix}$
Pauli-Y (Y)	$\boxed{Y}$	$\begin{bmatrix} 0 & -i \\ i & 0 \end{bmatrix}$
Pauli-Z (Z)	$\boxed{Z}$	$\begin{bmatrix} 1 & 0 \\ 0 & -1 \end{bmatrix}$
Hadamard (H)	$\boxed{H}$	$\frac{1}{\sqrt{2}}\begin{bmatrix} 1 & 1 \\ 1 & -1 \end{bmatrix}$
Controlled Not (CNOT, CX)		$\begin{bmatrix} 1 & 0 & 0 & 0 \\ 0 & 1 & 0 & 0 \\ 0 & 0 & 0 & 1 \\ 0 & 0 & 1 & 0 \end{bmatrix}$
Controlled Z (CZ)		$\begin{bmatrix} 1 & 0 & 0 & 0 \\ 0 & 1 & 0 & 0 \\ 0 & 0 & 1 & 0 \\ 0 & 0 & 0 & -1 \end{bmatrix}$
SWAP		$\begin{bmatrix} 1 & 0 & 0 & 0 \\ 0 & 0 & 1 & 0 \\ 0 & 1 & 0 & 0 \\ 0 & 0 & 0 & 1 \end{bmatrix}$

Table I: Set of important one-qubit and two-qubit gates with their gate and matrix representation.

qubit gate U is unitary if $U^\dagger U = I$, where $U^\dagger$ is the adjoint of U and a set of gates is universal if any quantum operation can be approximated to an arbitrary precision by a finite combination of those gates, as implied by the Solovay-Kitaev theorem [19].

The simplest one-qubit gate is the X-gate, which switches $|0\rangle$ to $|1\rangle$ and vice versa. The X-gate is also called the Pauli-X operator, and we can also use Pauli-Y and Pauli-Z operations as gates. Another important one-qubit gate is the Hadamard gate H which takes the state $|0\rangle$ to $\frac{1}{\sqrt{2}}(|0\rangle+|1\rangle)$ and $|1\rangle$ to $\frac{1}{\sqrt{2}}(|0\rangle-|1\rangle)$. Some important one-qubit and two-qubit gates are presented in Table I along with their matrix presentations. In this thesis, we also need rotation gates that can be parameterised.

A rotation of the state vector about the z-axis in Bloch sphere representation is given by the gate $R_z(\theta) = \exp(-iZ\theta/2)$. The matrix representation for it and other rotations are, following [17],

$$
\begin{aligned}
R_x(\theta) = \exp(-iX\theta/2) &= \begin{bmatrix} \cos(\theta/2) & -i\sin(\theta/2) \\ -i\sin(\theta/2) & \cos(\theta/2) \end{bmatrix}, \\
R_y(\theta) = \exp(-iY\theta/2) &= \begin{bmatrix} \cos(\theta/2) & -\sin(\theta/2) \\ \sin(\theta/2) & \cos(\theta/2) \end{bmatrix}, \\
R_z(\theta) = \exp(-iZ\theta/2) &= \begin{bmatrix} \exp(-i\theta/2) & 0 \\ 0 & \exp(i\theta/2) \end{bmatrix}.
\end{aligned}
\tag{3}
$$

From two-qubit gates the most important one is the controlled-NOT gate (CNOT). In the CNOT-gate, one qubit is the control qubit and the other one is the target qubit. If the control qubit is in the state $|0\rangle$, the target qubits stays unchanged and if it is in the state $|1\rangle$, the target qubit flips. In the circuit representation, the control qubit is marked as a filled dot and the target as an open circle, as seen in Figure I. Other gates can also be controlled , e.g., controlled-Z gate and controlled-$R_y(\theta)$ gate. SWAP gate switches the place of two qubits.

To obtain classical information from the quantum computation, the qubits are measured in some chosen basis. Usually, all qubits are measured at the end but, technically, they can be measured at any point during the computation. The measurement process collapses the quantum state and destroys the information stored in its superposition. The measurement is usually performed in the Z-basis but, by applying suitable gates before the measurement, any other basis can be chosen. The results are stored in classical bits and can then be analysed or used in subsequent conditional gates. [17]

The quantum computing platform used in this thesis is Qiskit, developed by IBM [18]. Qiskit provides the methods to create and perform simulations with quantum circuits either by using simulators on a local computer or real quantum devices

available in the cloud. Qiskit is provided as an open-source python package and includes many libraries that include different algorithms and tools. There are essentially two different kinds of local simulators. The *statevector simulator* simulates the ideal computation of a quantum circuit without any error or "shot noise", i.e., statistical fluctuations from limited number of measurements. The *qasm simulator* mimics more accurately the execution of a real quantum device, as it samples with finite amount of shots from the probability distribution of the quantum circuit which can lead to errors due to statistical fluctuations. It is also possible to set the *qasm simulator* to simulate the noise model of any real quantum device of IBM to mimic it more closely. Ideally, I would use *qasm simulator* for all analyses in this thesis, but due to limited amount of computing power and time, I will have to resort to using the *statevector simulator*, as is the common practice [18].

1.2 Exploring quantum systems with near term quantum algorithms

The main goal of this thesis is to introduce a method to investigate quantum properties of intermediate sized systems. This is done by combining two prominent algorithms, designed for near-term quantum computers that will be properly introduced later in their own chapters. Shortly, the Variational Quantum Eigensolver is used to find the ground state of the system under examination and then pairwise tomography is used to efficiently extract information from the ground state of the system. We are currently in an era in which our understanding of entangled quantum many-body systems is advancing and more advanced tools are required to extract and analyze information from them. These methods can also be used to study fundamental physics by using simple quantum models. A key property of these methods is their scalability. As better and larger quantum computers become available, these methods are ready to be used with arbitrarily large systems.

In the current NISQ era of 50-to-100 qubit devices, quantum supremacy has already been achieved [20, 21]. Quantum supremacy is another term coined by John Preskill, and it means that a quantum computer outperforms the best classical supercomputer at some task [22]. However, these particular tasks that have been used to achieve quantum supremacy are non-practical mathematical problems. In the near future, quantum supremacy with a practical application will most likely come from using a Variational Quantum Algorithm (VQA). VQA is a term for many different algorithms, which all have in common that they are designed to be used with limited number of noisy qubits in quantum computers with limited qubit connectivity and circuit depth. Common aspect of variational algorithms is that they are quantum-classical hybrid algorithms utilizing the best of both computation models. In a sense, they are analogous to classical machine learning neural networks with few key differences. In VQAs, the object to be optimized is a parametrized quantum circuit that is run on a quantum computer. The object function is also measured on a quantum computer, but the parameter optimization is done on a classical optimizer. [23]

1.2.1 Variational quantum eigensolver

In this thesis, I will be using a variational algorithm called Variational Quantum Eigensolver (VQE), the first of the variational algorithms ever developed [24]. VQE is used to calculate the eigenvalues and eigenvectors of a given system. Eigenvalues and eigenvectors are important for many systems, as they represent the ground and exited states of quantum systems. The ground state, especially, provides valuable information of the system's properties. Also, optimization problems can be mapped into Hamiltonians such that their lowest eigenvalue and the corresponding eigenvector represent the solution to the problem. In the future, the quantum phase estimation algorithm may be used to calculate minimum eigenvalues but it requires

more coherent and longer circuits than those implementable in the NISQ era [25]. In recent years, VQE has been heavily used in quantum chemistry applications because the ground state of an molecule provides valuable information such as the equilibrium bond length, bond angle, and dissociation energy [26–28]. There are potential benefits in drug discovery and studying other useful chemical reactions of e.g. new fertilizers that could lower the global carbon emissions by 2% [6, 7].

The focus here will be on simpler systems. These will be quantum spin chains and in particular, the quantum Ising model, the spin-1/2 XX chain and the XXZ model. These are chosen for their simple Hamiltonian and the fact that they have been extensively studied in the literature. In fact, the transverse Ising model has been called the fruit-fly of quantum many-body physics [29]. But before applying VQE to specific problems, I will first introduce the general formalism for VQE.

The first ingredient of the algorithm is the Hamiltonian H of the system. For physical applications, it gives the energy and time evolution of the system. Optimization problems can also be mapped to Hamiltonian form and then used with the VQE algorithm to find the lowest energy eigenstate, which then corresponds to the optimal solution to the problem. A distinction needs to be made between the system Q we are interested in and the physical system S that is doing the actual quantum computation. A requirement for the system S is that the number of qubits N in it is larger than or equal to what the system Q requires. The Hamiltonian of the system Q needs to be mapped to a system's S operator in order to perform the computation. If the systems are similar, this mapping is trivial but, in general, it is not. As an example, operators of fermionic systems can be mapped to qubits operators with the Jordan-Wigner transformation, which takes care of the fermionic commutation relations. Once the mapping is done we can use the system S to study the system Q we are interested in.

Consider an arbitrary state $|\psi\rangle$ and an arbitrary operator O. The expectation

value of this operator with respect to this state is

$$\langle O \rangle_{|\psi\rangle} = \frac{\langle \psi|O|\psi\rangle}{\langle \psi|\psi\rangle}. \tag{4}$$

Let us assume from now on that the wavefunction is normalized, $\langle \psi|\psi\rangle = 1$. [10]

In VQE, we want to measure the expectation value of the system's energy, which is done by calculating the expectation value of the system's Hamiltonian $\langle \psi|H|\psi\rangle$. Calculating this directly would require measuring it in the eigenbasis of the system which we actually do not know yet. Measurement in arbitrary basis can be done but is often hard and introduces many additional gates which is a problem in NISQ devices. Therefore, we solve this problem by decomposing the Hamiltonian into a polynomial sum of M operators that are easily measured by the quantum computer

$$H = \sum_{k}^{M} c_k H_k \tag{5}$$

with some complex coefficients c_k. The operators H_k are often chosen to be Pauli strings, which are tensor products of Pauli matrices and the identity operator, $P = \bigotimes_{j=1}^{N} \sigma_j^a$, where $\sigma_j^a \in \{I, \sigma_j^x, \sigma_j^y, \sigma_j^z\}$. Measuring σ^z is easy as it is just a measurement in the standard computational basis and measuring σ^x, σ^y requires only an addition of a one-qubit gate. Then the Hamiltonian is given by

$$H = \sum_{k=1}^{M} c_k P_k. \tag{6}$$

Now, the expectation value of the Hamiltonian decomposes into a weighted sum of expectation values of easily measurable Pauli strings [13]

$$\langle H \rangle_{|\psi\rangle} = \sum_{k}^{M} c_k \langle P_k \rangle_{|\psi\rangle}. \tag{7}$$

Next we need a parametrized quantum state that can be transformed into any state in some family of states. The state of the solution should be contained in this

family. The parametrized quantum circuit is formed by constructing a parametrized circuit called ansatz. This state is denoted with parameters $\boldsymbol{\theta}$ as $|\psi(\boldsymbol{\theta})\rangle$ and is obtained from the initial state $|\Psi_0\rangle$ with a unitary transformation $\mathcal{U}(\boldsymbol{\theta})$ as

$$|\psi(\boldsymbol{\theta})\rangle = \mathcal{U}(\boldsymbol{\theta})|\Psi_0\rangle. \tag{8}$$

The initial state is often just the computational basis state $|0\rangle^{\otimes N}$, but sometimes other initial states are more convenient. For example, in chemistry applications the Hartree-Fock approximation is usually a good starting place. To simplify, we can fuse the initial state preparation to the unitary evolution of the ansatz to obtain [13]

$$|\psi(\boldsymbol{\theta})\rangle = U(\boldsymbol{\theta})|0\rangle^{\otimes N}. \tag{9}$$

The eigenvalues of the Hamiltonian can be ordered as $\lambda_1 \leq \lambda_2 \leq \ldots \leq \lambda_N$. The lowest few eigenvalues are often the most interesting ones and we will focus on finding the lowest one, the ground-state energy. The variational theorem of quantum mechanics states that

$$\langle H \rangle_{|\psi(\boldsymbol{\theta})\rangle} = \langle \psi(\boldsymbol{\theta})|H|\psi(\boldsymbol{\theta})\rangle \geq \lambda_1. \tag{10}$$

No matter how we tweak the parameters $\boldsymbol{\theta}$, the expectation value of the Hamiltonian will not go below the lowest eigenvalue. Therefore, when trying to find the ground state of the system the optimal choice for the parameters $\boldsymbol{\theta}$ is the one which minimizes the expectation value of the Hamiltonian

$$\boldsymbol{\theta}_{\text{opt}} = \text{argmin}_{\boldsymbol{\theta}} \langle \psi(\boldsymbol{\theta})|H|\psi(\boldsymbol{\theta})\rangle. \tag{11}$$

The approximation to the ground state energy will be then $E_{\text{opt}} = \langle \psi(\boldsymbol{\theta}_{\text{opt}})|H|\psi(\boldsymbol{\theta}_{\text{opt}})\rangle$ and approximation to the ground state $|\psi(\boldsymbol{\theta}_{\text{opt}})\rangle = U(\boldsymbol{\theta}_{\text{opt}})|0\rangle^{\otimes N}$. [13]

We now have the tools to describe the VQE algorithm. First, we prepare the ansatz $|\psi(\boldsymbol{\theta})\rangle$ on a quantum computer. There are many different choices of ansatz
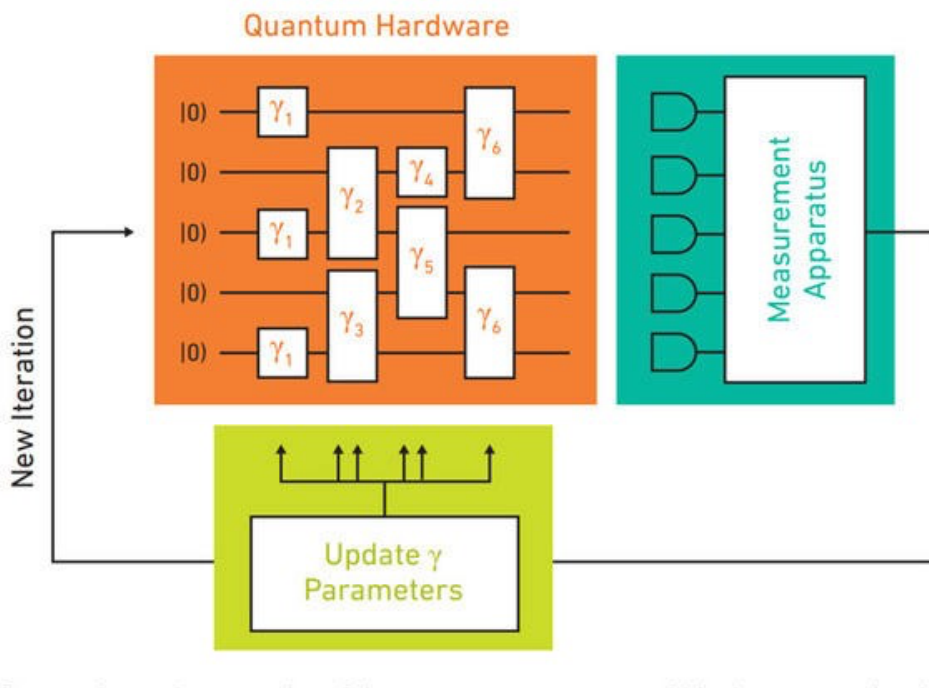
Figure 2: An illustration of one VQE cycle. If it is the first iteration, the parameters of the ansatz are initialized in some random or predetermined state. Otherwise, parameters from previous iteration are used. The objective function is then measured respect to the state of the ansatz. The results are sent to a classical optimizer that determines how to adjust the parameters such that the measurement value would decrease in the next iteration. The new parameters are then updated in the ansatz and the algorithm enters the next iteration. The cycle halts when some criteria for the convergence has been met. Usually it is when the variance of the measurement expectation value decreases below a certain limit. The figure is extracted from [30].

depending on the hardware and the system under study. Next, we measure the expectation value of the Hamiltonian $\langle H \rangle_{|\psi(\boldsymbol{\theta})\rangle}$ with respect to this state. Then, these values are used with classical optimizer algorithm to determine how the parameters of the ansatz $\boldsymbol{\theta}$ need to be changed in order to decrease $\langle H \rangle_{|\psi(\boldsymbol{\theta})\rangle}$. There are many different options for the optimizer. These new parameters are then updated in

the ansatz and the algorithm continues to a new iteration. This is repeated until convergence i.e. when variation of the expectation value $\langle H \rangle_{|\psi(\boldsymbol{\theta})\rangle}$ decreases below a desired limit. The VQE cycle is shown in Figure 2. [10]

Ansätze can be dived into two groups: problem-inspired ansätze and hardware-efficient ansätze. In problem-inspired ansätze the parametrized quantum circuit is constructed with generators that are derived from properties of the system of interest. In quantum chemistry, for example, the unitary coupled-cluster approach is often used [31]. Problem-inspired ansätze are problem specific and can be efficiently trained in those specific problems. However, they often require deep and highly connected circuits and thus require hardware we currently do not have. Hardware-efficient ansätze accommodate the constraints of current technology. They are constructed with a limited set of quantum gates and limited connectivity. The gate set consists usually of few single-qubit gates and one two-qubit entangling gate, e.g. a CNOT gate. These are used to construct a layer of circuit that can then be repeated as many times as necessary. Hardware-efficient ansätze are shallower than problem-inspired ansätze but they can suffer from trainability issues. [13, 23]

Important for an ansatz is its entangling power which measures the set of states it can represent [32]. If the ansatz can prepare any state in the Hilbert space then the solution state is guaranteed to be there, however, finding it might be a hard task. Problem-inspired ansätze limit the set of states they can represent, which is one of the reasons they converge faster to the solution state. Hardware-efficient ansätze can be made to represent an arbitrarily large amount of states, as guaranteed by the Solovay-Kitaev theorem. Any state can be generated by some unitary transformation applied to the initial state and this theorem states that an arbitrary unitary acting on n qubits can be approximated with precision ε by using at most order $\Theta(\log^c(1/\varepsilon))$ elementary gates from an universal gate set. Θ is used to describe the growth rate of a funtion. The value for c depends on the proof for
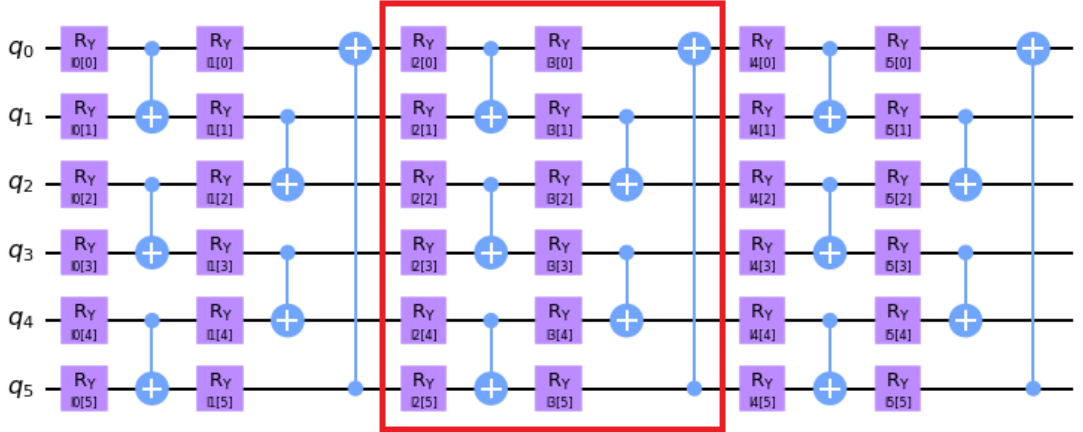
Figure 3: Variational hardware-efficient layered ansatz with six qubits and three layers. The red box indicates one layer of the ansatz with parametrized $R_y(\theta)$ rotations and entangling CNOTs.

this theorem but it is known to lie between $1 \leq c \leq 4$. [32]

The ansatz layout that is used in this thesis is a hardware-efficient layered ansatz, which can be seen in Figure 3. The ansatz is constructed from subsequent layers of single-qubit gates and entangling two qubit-gates. The single-qubit gates are all parametrized $R_y(\theta)$ gates, and the two qubit gates are entangling CNOTs. Inside one layer, the rotation gates and CNOTs are alternated and, furthermore, the control and target qubits of CNOTs change. This circuit can be interpreted as the Trotter approximation to the unitary $U(\boldsymbol{\theta})$ of Equation (9), which takes the state $|0\rangle^{\otimes N}$ to the parametrized state $|\psi(\boldsymbol{\theta})\rangle$ [32]. The parametrized $R_y(\theta)$ gates are chosen because the operations are real (no imaginary components) and the Hamiltonians (see equations (14), (15) and (16)) of interest are also real. The entangling power of this circuit can be adjusted by adding more layers to it. The more layers are added, the more accurately it can approximate the ground state of the system under study. As every layer adds a CNOT between all pairs of adjacent qubits, adding a layer creates one bit of entanglement per pair and per layer. [32]

Choosing the right optimization method is critical for the success of the VQE

algorithm. The inspiration for these methods is taken from classical optimizers, and many are exactly the same. However, there are new challenges due to the quantum nature of the problems, such as the stochastic environment due to limited measurements, hardware noise, and barren plateaus (regions of non-convergence) [33]. Therefore, more quantum-aware optimizers have been developed but no clear winner has been found yet. Optimizers can be broadly grouped into two categories, depending on whether they use some kind of gradient descent method or not. Gradient descent methods optimize by taking iterative steps into the direction of the gradient. Sequential Least Squares Programming optimizer (SLSQP) is an example of an iterative method that works well for problems where the objective function and the constraints are twice continuously differentiable. When working with statevector simulator, SLSQP is the optimizer that is used in this work. [23]

Because of the limited number of measurements, quantum algorithms actually use Stochastic Gradient Descent methods (SGD). An example of a SGD method is Adam [34]. The other methods do not directly utilize gradients, and an example of such is the Simultaneous Perturbation Stochastic Approximation (SPSA) method [35]. SPSA approximates the gradient by calculating a single partial derivative along randomly chosen direction. The partial derivative is computed as a finite difference, and therefore requires only two measurements of the objective function. SPSA is an optimal choice to be used with a *qasm simulator* or a real quantum device, as it can be used in the presence of noise and uncertainty in the measurement [18]. Based on these considerations and also on experiments, SPSA was chosen as the optimizer to be used in this thesis when working with *qasm simulator*. [23]

It is important to know when to stop the iteration of the VQE algorithm. Earlier, I mentioned that the iteration is continued until the variance of the expectation value decreases below certain limit, and this can be made more precise. In density matrix formalism, the expectation of an arbitrary operator O for a state ρ is given

as $\langle O \rangle_\rho = \text{Tr}[\rho O]$. The variance of an arbitrary operator is then given as $\text{Var}[O]_\rho = \langle (O - \langle O \rangle_\rho)^2 \rangle_\rho = \langle O^2 \rangle_\rho - \langle O \rangle_\rho^2$. Now, for any eigenstate $|\Psi_k\rangle$ the variance of any operator O is

$$\langle \Psi_k | O^2 | \Psi_k \rangle - \langle \Psi_k | O | \Psi_k \rangle^2 = (\lambda_k^2) - (\lambda_k)^2 = 0. \tag{12}$$

Therefore, when converging near an eigenstate, we can aim at decreasing the variance of the energy as much as possible and for any approximate eigenstate $|\tilde{\Psi}\rangle$ we have that [10]

$$\text{Var}[O]_{|\tilde{\Psi}\rangle} \geq 0. \tag{13}$$

1.2.2 Quantum spin chains

Now we are going to look at specific models and how to apply VQE to simulate them. Our three quantum systems are the Ising model in transverse field, the spin-1/2 XX chain and the XXZ model. These three systems and their properties will be analyzed in the remaining thesis. The Hamiltonian for the Ising model is

$$H_{\text{Ising}} = -J \sum_{i=1}^{N} \left[\sigma_i^z \sigma_{i+1}^z + B \sigma_i^x \right], \tag{14}$$

where B is the strength of the transverse magnetic field and we set $J = 1$ without loss of generality. The spin chain is set to have open boundaries, so $\sigma_{N+1}^z = 0$. For small values of B ($B < 1$), the ground state of the system is in a degenerate and ferromagnetic phase where all the spins are in a GHZ like superposition of all spins aligned in the positive z direction and in the negative z direction. For large values ($B > 1$) the system is in paramagnetic phase and the spins are in disorder. In both phases the Hamiltonian is gapped i.e there is a finite difference between the ground state energy and the first exited state energy. Note that for $B < 1$ the ground state is degenerate, so the gap is actually between the second and the third

smallest eigenvalues. The system has $\mathbb{Z}_2$ symmetry in both phases so that applying spin flip to all spins $\prod_j \sigma_j^x$ does not change the energy of the system. At exactly $B = 1$ the system is in critical phase and the $\mathbb{Z}_2$ symmetry breaks spontaneously. The physics of the system is very different in the critical phase and in other phases. The main aspect that is important in this thesis is that the paramagnetic phase is shortly correlated and gapped and so fulfills the area-law of entanglement. The ferromagnetic phase is partly gapped but exhibits long range correlations and the critical phase is gapless and also exhibits long range correlations. This will be elaborated in later sections. [32]

The spin-1/2 XX model has the following Hamiltonian

$$H_{XX} = J \sum_{j=1}^{N} \left[\frac{1}{2}(\sigma_i^x \sigma_{i+1}^x + \sigma_i^y \sigma_{i+1}^y) + B\sigma_i^z \right], \tag{15}$$

where again B is the strength of the magnetic field, J is set to unity, and open boundaries are fixed using $\sigma_{N+1}^{x,y} = 0$. For $B > 1$, the ground state of the system is aligned along the z direction and separable. The system undergoes a quantum phase transition at $B = 1$ to a critical phase in the thermodynamical limit. Between $0 < B < 1$ the system is critical and it undergoes N level crossings at magnetic field values $B_k = \cos[k\pi/(N+1)]$, with $1 \leq k < N$. Above $B > 1$ all spins are aligned in the z direction. At each crossing, one of the spins, that already has not, gets flipped and the result is a highly entangled state, given as a symmetric superposition of all possible flips. [9, 36]

The XXZ model has the following Hamiltonian

$$H_{XXZ} = J \sum_{j=1}^{N} \left[\sigma_i^x \sigma_{i+1}^x + \sigma_i^y \sigma_{i+1}^y + \Delta\sigma_i^z \sigma_{i+1}^z \right], \tag{16}$$

where J is again set to unity, open boundaries are set, $\sigma_{N+1}^{x,y,z} = 0$, and Δ is now the spin anisotropy. This system is gapped for $\Delta \gg 1$ and $\Delta \ll -1$ being ferromagnetic for $\Delta < -1$ and anti-ferromagnetic for $\Delta > 1$ along the z direction. Between $-1 \leq \Delta \leq 1$, the system is critical, and describes the physics of a compactified

boson. All models, the Ising, the spin-1/2 XX and the XXZ model, in critical phase can be described with a conformal field theory (CFT) with different central charges [37, 38]. [32]

1.2.3   Depth scaling of the VQE ansatz

To benchmark the VQE algorithm I will study the scaling of the accuracy in terms of the ansatz depth. I do this by using the Ising model with values of $B = 0.5, 0.8, 1.0, 2.0$ and 10.0 for the magnetic field and the hardware efficient ansatz discussed previously. The simulation is done using the *statevector simulator*. The accuracy is evaluated with two quantifiers and the first one is the accuracy of the ground-state energy δ_E evaluated with the formula $\delta_E = \log_{10}(\frac{1}{\epsilon})$, where $\epsilon = E_{\mathrm{VQE}} - E_{\mathrm{exact}}$, with E_{exact} the true ground state energy calculated by diagonalizing the Hamiltonian exactly and choosing the lowest eigenvalue, and E_{VQE} is the energy achieved with VQE. The second quantifier is the fidelity of the exact diagonalized state ρ_{exact} and VQE state ρ_{VQE} calculated as $F\left(\rho_{\mathrm{exact}}, \rho_{\mathrm{VQE}}\right) = \mathrm{Tr}\left[\sqrt{\sqrt{\rho_{\mathrm{exact}}}\rho_{\mathrm{VQE}}\sqrt{\rho_{\mathrm{exact}}}}\right]^2$.

The results for the scaling of the accuracy of the ground-state energy, and fidelity as a function of circuit depth can be seen in Figures 4 and 5, respectively. From both graphs, it can be seen that for lower values of magnetic field, the convergence towards ground state is slower and requires higher ansatz depth. The graph for fidelity more clearly shows the limit point for finding a good approximation for the ground state. The systems with magnetic value above one immediately approach the ground state but for systems with $B \leq 1$ it takes a certain amount of layers. With the exception of the case of $B = 0.5$, they all converge to ground state eventually. For large amounts of layers, the accuracy is approximately the same in all cases.

The figure for accuracy matches, in essence, the results of systems with $B > 1$ to the results of Bravo-Pierto et al. [32] although the numbers do not exactly match because of different system sizes. Moreover, they consider spin chains with periodic
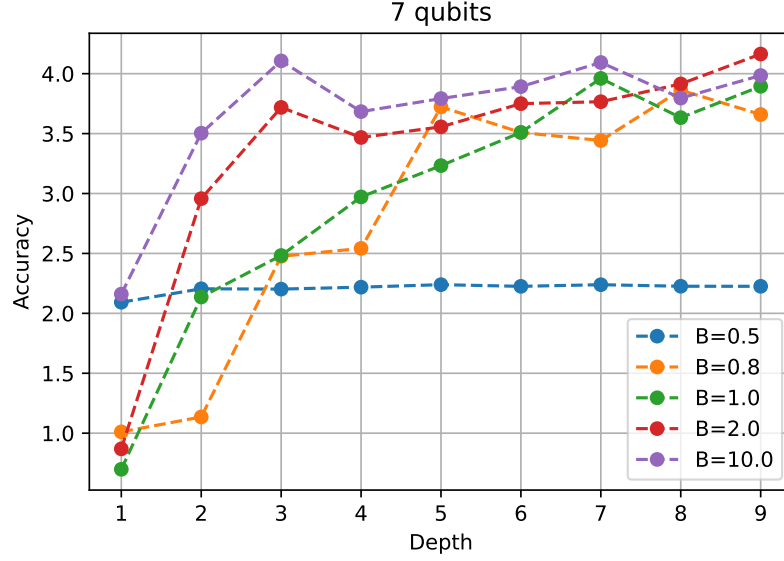
Figure 4: The scaling of accuracy of the ground state energy, δ_E, for different magnetic field values, B. The magnetic field is rescaled by J. The x-axis depicts the number of layers in the ansatz. The graph illustrates how many layers are needed for a given magnetic field value to achieve good convergence. Cases with higher B need fewer layers to achieve good accuracy. The case with $B = 0.5$ does not converge with the number of layers presented here.

boundary conditions. One of the results of that paper is that the accuracy of the energy for Ising model with $B > 1$ increases exponentially as a function of the ansatz depth. For the critical phase, $B = 1.0$, the accuracy is first in a *finite-depth* regime and stays constant until the depth of the circuit crosses a limit point, after which it enters into a *finite-size* regime where the accuracy increases exponentially. The limit point scales linearly with the number of qubits. However, no analysis was done for systems with $B < 1$ and the behaviour was explained to happen with systems in the critical phase. Here I find new results that the same behaviour happens for all Ising model systems with $B < 1$ and more strongly for lower B. As seen later in Figure 23, the energy gap in the Hamiltonian might be one of the causes behind
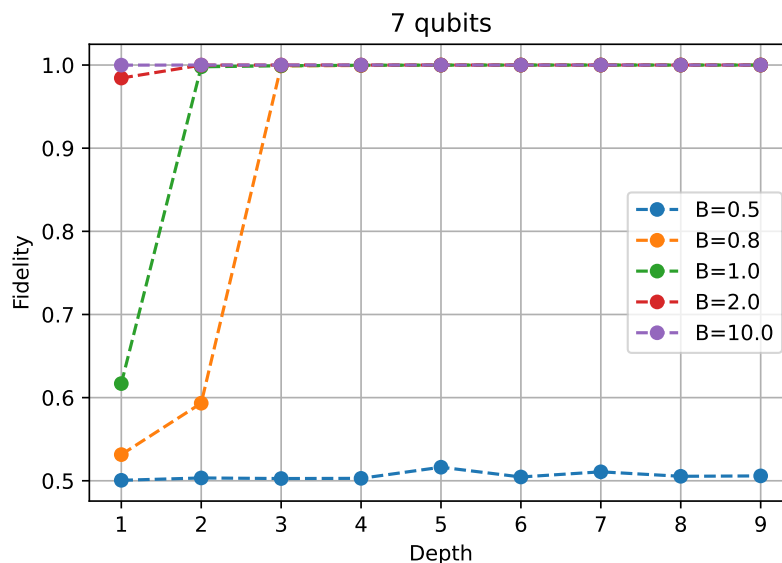
Figure 5: The scaling of fidelity of the VQE ground state and exactly diagonalized ground state for different magnetic field values, B. The magnetic field is rescaled by J. The x-axis depicts the number of layers in the ansatz. The graph is similar to Figure 4, but illustrates even more clearer how many layers are needed for a given magnetic field value to achieve good convergence. Cases with higher B need fewer layers to achieve good accuracy. The case with $B = 0.5$ does not converge with the number of layers presented here.

this behaviour. By testing the convergence of the Ising model for different magnetic fields, it was noted that finding the ground state for systems with $B < 0.5$ was much harder and required much deeper ansätze than for other values. This behaviour will be investigated more in depth in future work.

1.2.4 Pairwise quantum tomography

Now that we have the means to find the ground state of a given system, how can we extract information out of it? The state is stored in a parametrized circuit, which we can initialize as many times as we want, but we still do not know much about

its properties other than its energy. If we were to have an explicit description of its state vector or density matrix, we would be able to calculate any interesting quantity from it. The process of reconstructing a quantum state from an ensemble of measurements in different bases is called quantum state tomography. As measurement destroys the quantum information, the state needs to be initialized again after every measurement process. Luckily, with our parametrized quantum circuit this is not hard although errors during initialization may happen. This kind of full state tomography presents two problems: it requires exponential amount of measurements with increasing system size and the result is a matrix which requires exponential amount of storage capacity with increasing system size. [11]

A more efficient method is to perform pairwise tomography instead of full state tomography. By measuring just pairwise correlators with a clever measuring scheme, the scaling reduces from exponential number of measurements to just logarithmic number of measurements in terms of system size. It does not contain all the information, as full state tomography would, but we do obtain interesting pairwise quantities that are enough to study some relevant properties of the system. Examples of quantities that one can extract are pairwise entanglement, mutual information, classical correlations, von Neumann entropy, quantum discord and purity. [11]

To construct pairwise density matrices we need to calculate correlators of the form $\langle \sigma_i^a \otimes \sigma_j^b \rangle$ between all pairs of qubits, (i, j), with a and b taking values x, y and z. Hence, calculating all pairwise correlators, for a pair of qubits involves measuring 9 different correlators and for all pairs this amounts to measuring $9N(N-1)/2$ observables. With simple parallel measurements this is reduced by a factor $\lfloor N/2 \rfloor$, so that it can be done in $\mathcal{O}(N)$ measurements setups, but a better method will be shown next to reduce it to $\mathcal{O}(\log N)$. [11]

The easiest part is measuring correlators $\langle \sigma_i^a \otimes \sigma_j^a \rangle$, where the measurement basis is the same for both qubits. This is done with three measurement setups, first

measuring all qubits in the x basis, then y and lastly z. For all other correlators, we need an efficient scheme that ensures that all non-trivial correlators are covered. In this scheme, qubits are repeatedly assigned letters a, b and c which mark the different combinations of measurements that will be done, as explained below. [11]

Each qubit is first indexed from 0 to $N - 1$. In base three representation, these indexes use $\lceil \log_3 N \rceil$ digits. We use $\lceil \log_3 N \rceil$ labellings, $l = 1, \ldots, \lceil \log_3 N \rceil$, where each labelling is such that it assigns for each qubit i the letter a, b or c based on the value of its l-th digit in its base-three representation. An example makes this clearer. Consider a system of 15 qubits indexed $0, \ldots, 14$, so the number of labellings is $L = \lceil \log_3 15 \rceil = 3$. Then, the index of its 12th qubit, 11, is presented in base three as 102_3. Then for labelling $l = 1$, the 12th qubit would be assigned the letter c, for labelling $l = 2$, the letter a, and for labelling $l = 3$, the letter b. After this, the letters a, b, c are substituted by the six different permutations of x, y and z, and the corresponding measurements are performed. Generally, as any two qubits have different indexes and therefore at least one distinct digit in the base-three representation, it is guaranteed that every pair of qubits will have at least one labelling where their non-trivial correlators will be measured. Furthermore, this scheme is optimal. [11]

With 3 trivial measurement settings of the same basis and 6 setting per labelling, the total number of measurement settings is

$$6\lceil \log_3 N \rceil + 3. \tag{17}$$

In this thesis I will cover systems of sizes between 6 and 12. For $N = 12$ qubits the total number of measurement settings with this scheme is 21. The naïve parallel approach would have required $(9 \times 12 \times (12 - 1)/2)/(\lfloor 12/2 \rfloor) = 99$ measurement settings. The difference is huge even for small systems, and even more so with increasing system size. [11]

The algorithm is then the following. First perform the three measurements where
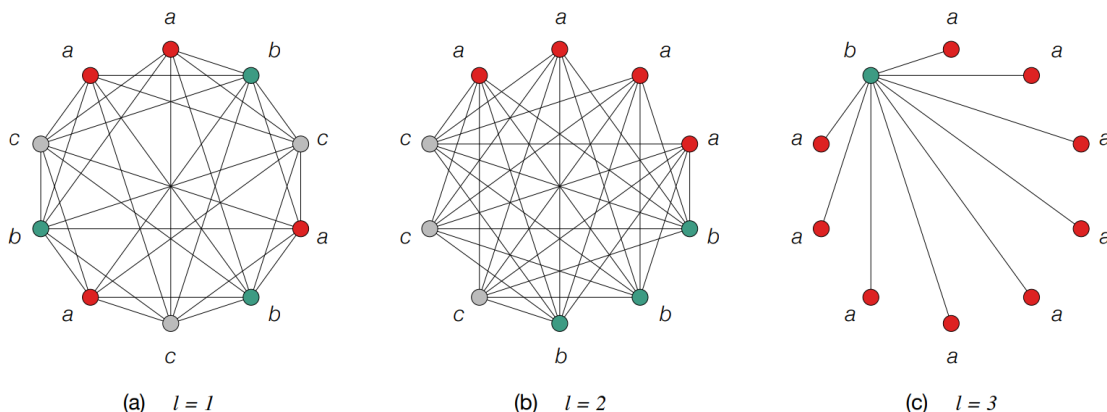
Figure 6: Groupings of the pairwise tomography algorithm for $N = 10$ qubits. Here there are $L = \lceil \log_3 10 \rceil$ labellings. The top-most qubit is the first qubit with index i=0 and counting continues clockwise. Each qubit is assigned letter a,b and c according to the result of $\lfloor i/3^{l-1} \rfloor$ mod 3. [11]

all qubits are measured in the same basis x, y, and z. Then, calculate the number of labellings needed $L = \lceil \log_3 N \rceil$ and for each $l = 1, \dots, L$ do the following substeps: a) First divide the qubits into groups of subsequent 3^{l-1} qubits and for each group assign cyclically $a, b, c, a, b, \dots$. The last group may have fewer qubits than other groups. b) Then assign all permutations of x, y and z to letters a, b and c:

$$
\begin{array}{ccccccc}
 & & 1 & 2 & 3 & 4 & 5 & 6 \\
a & \longleftarrow & x & x & y & y & z & z \\
b & \longleftarrow & y & z & x & z & x & y \\
c & \longleftarrow & z & y & z & x & y & x
\end{array}
\tag{18}
$$

and for all permutations perform measurements as indicated by the assigned letter. An example for this algorithm can be seen in figure 6 for $N = 10$ qubits. [11]

After all measurements are performed, the results are used for the tomographic reconstruction of the reduced density matrices for all pairs of qubits. This can be done in various ways such as simple linear inversion or Bayesian methods. The code used in this thesis uses Qiskit's tool, which employs a maximum-likelihood method.
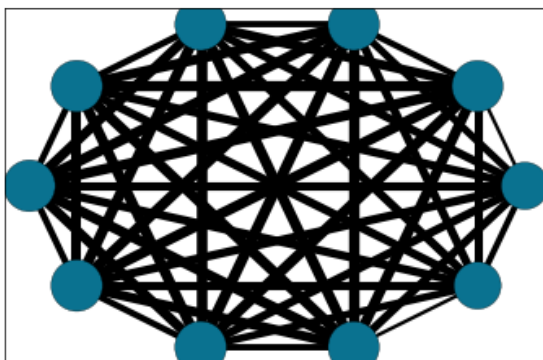
Figure 7: Pairwise entropies for the Ising model with 10 spins and $B = 1.5$. The magnetic field is rescaled by J.

[11]

1.2.5 Quantifiers of pairwise correlations for quantum systems

We now have the tools to obtain pairwise information from quantum systems, but what are the properties that we are interested in? There are many different quantifiers to characterize a quantum system, and in this thesis we are mainly interested in two of them: quantum mutual information, and concurrence. Because the properties that are to be investigated here are extracted from the system using the introduced pairwise tomography method, the quantifiers are all pairwise, i.e., they are calculated from two-qubit reduced density matrices. [11]

A key concept in quantum information theory is entropy. Shannon entropy is familiar from statistical mechanics and has multiple interpretations. It can measure the uncertainty of a random variable before we learn about it, or it can quantify the amount of information we would get by measuring it. From an information theory perspective, the most interesting interpretation is that entropy measures the amount of physical resources needed for storing and also transporting information. There is a corresponding quantity for quantum states with similar interpretations called Von

Neumann entropy, defined for state ρ as

$$S(\rho) \equiv -\text{tr}(\rho\log(\rho)). \tag{19}$$

Here, and later on, the logarithm is taken to be base two. Also, from now on, entropy always refers to Von Neumann entropy. If λ_k are the eigenvalues of ρ, then

$$S(\rho) = -\sum_k \lambda_k \log \lambda_k. \tag{20}$$

While having similar interpretations as the classical entropy, quantum entropy is still fundamentally different. Classical entropy originates from lack of knowledge in thermal states, while quantum entropy originates from quantum entanglement, and even at zero temperature, states with non-zero entropy are common [39].

Pairwise entropy for qubits a and b is calculated from the reduced density matrix ρ_{ab} as

$$S(\rho_{ab}) = -\text{tr}(\rho_{ab}\log(\rho_{ab})), \tag{21}$$

where ρ_{ab} is calculated by tracing out the other qubits of the system S as $\rho_{ab} = \text{tr}_{S/\{a,b\}}(\rho)$. An example of an pairwise entropy network can be seen in Figure 7 for the Ising model with 10 spins and $B = 1.5$. [17]

Classical mutual information measures how much common information two random variables X and Y have in common. The quantum analog carries a similar meaning but it also includes quantum correlations. For a bipartite quantum system ρ_{AB} (a quantum system with two parts) quantum mutual information is a measure of correlation between those two parts and it is defined as

$$S(A:B) = S(A) + S(B) - S(AB), \tag{22}$$

where $S(A)$ and $S(B)$ are the entropies of the reduced subsystems ρ_A and ρ_B, and $S(AB)$ is the entropy of the complete system. For pairwise mutual information,
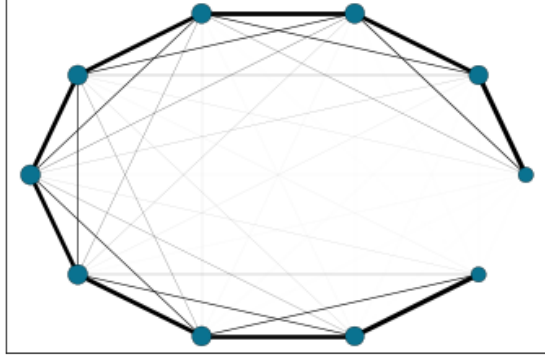
Figure 8: Pairwise mutual informations for the Ising model with 10 spins and $B = 1.5$. The magnetic field is rescaled by J.

the complete system AB is the reduced two-qubit system, and A and B are single qubits. An example of a pairwise mutual information network can be seen in Figure 8 for the same system as previously. [17]

Many relevant physical properties of ground states of quantum spin chains can be inferred from pairwise quantities such as mutual information. One interesting topic is the study of Quantum Phase Transitions (QPT) which are often characterized with two-point correlators of the form $g_{ij}^{(2)} = \langle \sigma_i^z \sigma_j^z \rangle - \langle \sigma_i^z \rangle \langle \sigma_j^z \rangle$. However, it is not generally know a priori what the right correlators are. The mutual information $S(A : B)$ gives upper bound to any two-point correlator as [8]

$$S(A : B) = S\left(\rho_{AB} \| \rho_A \otimes \rho_B\right) \tag{23}$$

$$\geq \frac{1}{2} \left| \rho_{AB} - \rho_A \otimes \rho_B \right|^2 \tag{24}$$

$$\geq \frac{\left\{ \mathrm{Tr}\left[\left(\rho_{AB} - \rho_A \otimes \rho_B \right) \left(\mathcal{O}_A \mathcal{O}_B \right) \right] \right\}^2}{2 \left\| \mathcal{O}_A \right\| \left\| \mathcal{O}_B \right\|^2} \tag{25}$$

$$= \frac{\left(\langle \mathcal{O}_A \mathcal{O}_B \rangle - \langle \mathcal{O}_A \rangle \langle \mathcal{O}_B \rangle \right)^2}{2 \left\| \mathcal{O}_A \right\|^2 \left\| \mathcal{O}_B \right\|^2}. \tag{26}$$

As the mutual information is a more general quantifier than any particular physical correlator, it is a suitable tool for analysing QPT [29].

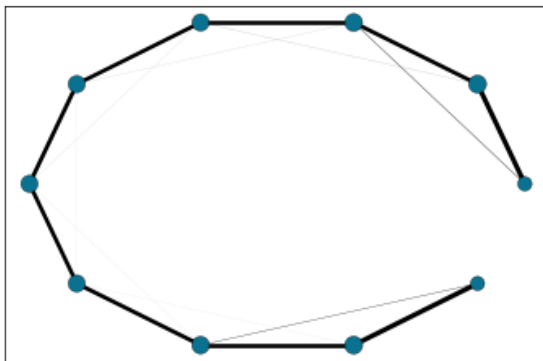Concurrence is a measure of entanglement that can be used to calculate the

Figure 9: Pairwise concurrences for the Ising model with 10 spins and $B = 1.5$. The magnetic field is rescaled by J.

entanglement of formation. Entanglement of formation is an entanglement measure that quantifies the resources needed to create a given entangled state and is an important quantity in analyzing entanglement. However, concurrence is in its own right a good measure of entanglement and so I will focus only on it. To calculate concurrence, we first need to do a spin flip transformation to the state, which for a density matrix of two qubits is calculated as

$$\tilde{\rho} = (\sigma^y \otimes \sigma^y)\rho^*(\sigma^y \otimes \sigma^y), \tag{27}$$

where ρ^* is the complex conjugate taken in the standard basis. The concurrence is then calculated as

$$C(\rho) = \max\{0, \lambda_1 - \lambda_2 - \lambda_3 - \lambda_4\}, \tag{28}$$

where λ_i are the eigenvalues of the Hermitian matrix $R \equiv \sqrt{\sqrt{\rho}\tilde{\rho}\sqrt{\rho}}$, in decreasing order. Concurrence is an entanglement monotone. It is a non-negative function, zero only for separable states and it does not increase under Local Operations and Classical Communications (LOCC). An example of a concurrence network can be seen in Figure 9, again for the same system as previously. [40, 41]

2 Emergent entanglement phenomena in quantum systems

Emergent quantum entanglement structures in quantum many-body systems is a rich and interesting research area that has seen increasing interest in the last decades. Advancements in these topics impact relatively new fields such as quantum biology, quantum thermodynamics, and more established fields such as quantum chemistry and quantum gravity. More obvious impact areas are, of course, quantum technologies, quantum computing, quantum internet, and quantum simulations that can be used for researching drugs and materials. The key conceptual ingredient binding all these topics is emergent phenomena and behaviour. These are properties that cannot be reduced to or be derived from laws governing the smaller parts of the system. Instead, one has to study complex collective structures that arise from a large number of individual interacting systems. [9]

Entangled quantum many-body states are complex structures that require advanced methods in order to study them. In the past, classical statistical physics has offered powerful tools for analyzing complex classical systems, including the study of complex networks. These have been used in quantum systems, but with the approach of explicitly enforcing complex structures on quantum connections [29]. An alternative approach is to combine the powerful instrument of quantum information with network representations to describe complex many-body quantum states and this is the approach taken in this thesis. [9]

The unique combination of methods introduced in this thesis allows for efficient analysis of quantum entanglement structures. Normally one would use a classical computation method, such as the MPS approximation, to perform the numerical calculations needed to find the ground state of the system of interest and extract its properties [42]. The method presented here does not suffer from the limitations

that MPS have: bad scaling in terms of entanglement and system size. Instead, it scales to arbitrary system size and amount of entanglement with the development of suitable quantum devices. VQE will find the desired ground state or exited state and pairwise tomography will extract the necessary pairwise quantities to construct the complex entanglement networks to then be analysed.

Two different analyses will be done in the remaining of this thesis. In the first part, I analyze the topological properties that emerge from entanglement networks of quantum many-body systems. In the second part, I study the application of the methods for studying quantum gravity and emerging space from entanglement. The analysis is done using the three already introduced quantum spin chains with equations (14), (15) and (16). The Ising model and the spin-1/2 XX chain have been extensively studied in references [9], [29] and [36], and the goal is to match their results to benchmark the methodology. These papers have used large amount of spins in their analyses, which needs to be taken into consideration when comparing the results. For the XXZ spin chain, I will present new results.

2.1   Topological properties of quantum many-body systems

It is now clear that we have great motivations to study the entanglement properties of quantum many-body systems. If we understand how entanglement works in relatively simple systems, then we can apply that knowledge to harder and more complex problems. Even in simple and extensively studied systems, we can find new and interesting emergent phenomena. With the three spin chain models I will study (i) the effects of being in and near the critical phase of the model, (ii) the emergent entanglement structures, (iii) scaling of the entanglement in different parts of the spin chain and (iv) network properties of the entanglement networks. [9]

These phenomena are studied with the use of complex networks, where the links represent either mutual information or concurrence. Mutual information measures

all correlations of the system, quantum and classical, which gives a good overall picture of the properties of the system. If one wants to study only entanglement phenomena, then concurrence is a more suitable quantifier. Pairwise concurrence networks show how the entanglement is distributed in the system.

2.1.1 Complex networks

To analyze the pairwise networks of quantum information properties that we obtain from the introduced methods, we need key concepts of network theory that I will now introduce. Complex networks are tools to represent complex systems as graphs, where nodes are individual systems and the links represent different relationships between them. Classical examples are social networks and internet connections. Graphs of complex networks can be visually presented for easy reading, but only when the number of subsystems is small enough that they do not clutter the view. Complex networks can be described with properties that give a holistic view of the whole system. These properties only emerge from the combination of the subsystems and cannot be reduced into microscopic rules that govern them. These properties are even more useful for describing networks where the number of subsystems is too large for visualization. In this thesis, the individual systems will be single spins and the links will represent the pairwise quantities that are extracted from the system using pairwise tomography. As the system sizes are small, everything can be visualized in addition to the quantitative analysis. [43]

The simplest quantity is the degree of a node. It measures the number of links that intersect the node without considering the weights of the links. Let us denote an arbitrary quantity of a weight between nodes i and j as ω_{ij} which can be e.g. concurrence or mutual information. Then, the presence of a link is denoted by $a_{ij} = \Theta(\omega_{ij})$ where Θ is the Heaviside function, so $a_{ij} = 1$ if a link exists between i

and j and $a_{ij} = 0$ otherwise. The definition for the degree of a node i is then

$$d_i = \sum_{j=1}^{N} a_{ij}. \tag{29}$$

Node degrees quantify the properties of the unweighted structure of the network, also referred to as its topology. A similar quantity, which is called the strength of the node i, is

$$s_i = \sum_{j=1}^{N} \omega_{ij}. \tag{30}$$

This quantifies the weighted structure of the network. [9, 29]

The local clustering coefficient counts the ratio of triangles i.e. three nodes with all three links present, to triples with at least two links present, in an unweighted network

$$c_i = \frac{\sum_{j,k}^{N} a_{ij} a_{ik} a_{jk}}{d_i(d_i - 1)}. \tag{31}$$

For a weighted network, this is instead

$$c_i^{\omega} = \frac{\sum_{j,k}^{N} (\omega_{ij} \omega_{ik} \omega_{jk})^{1/3}}{d_i (d_i - 1) \max_{lm} \omega_{lm}}, \tag{32}$$

where the geometric mean of each triangle is calculated and normalized with the largest weight in the whole network. [9]

The density D of the network is the weighted fraction of all the possible $\binom{N}{2}$ links that actually are present in the network

$$D = \frac{\sum_{i}^{N} s_i}{N(N - 1)}. \tag{33}$$

A network is said to be sparse if $D \to 0$ as $N \to \infty$ and dense otherwise. [29]

The disparity Y_i of a node i quantifies the heterogeneity of the distribution of its connections' weights as

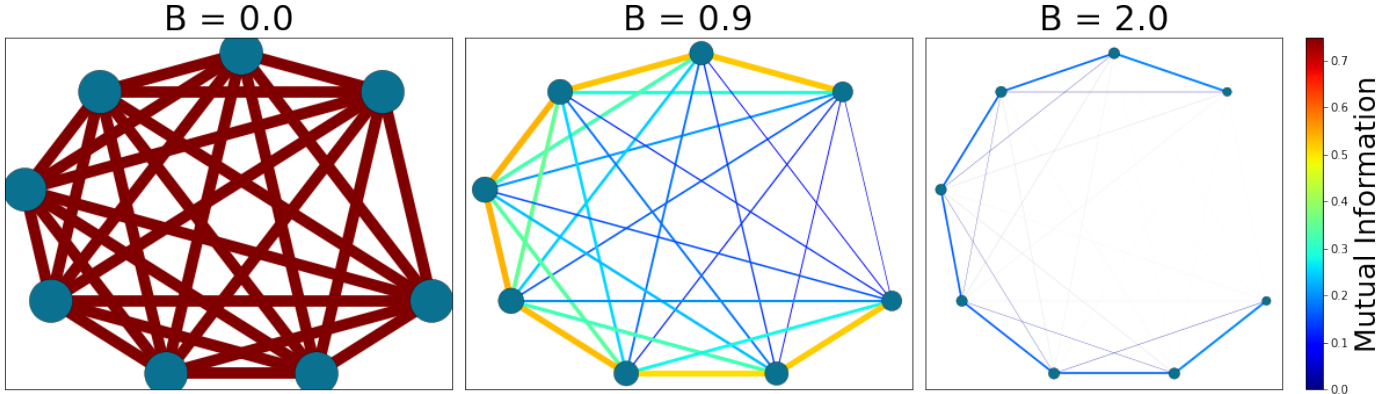$$Y_i = \frac{1}{s_i^2} \sum_{j=1}^{N} (\omega_{ij})^2. \tag{34}$$

Figure 10: Mutual information networks for the Ising model with three different magnetic field values B. The magnetic field is rescaled by J.

For a uniform distribution of the weights of node i, the disparity is $Y_i = 1/d_i$ and it approaches 1 if one of the links dominates. The average disparity over the whole network is then $Y = \frac{1}{N}\sum_{i=1}^{N} Y_i$. It is a good indicator of how the links are distributed across the network. [29]

2.1.2 The Ising model

First I will analyze the Ising model, as it is the simplest of the spin chains. The Hamiltonian for the Ising model was introduced in Equation (14). Recall that it is ferromagnetic for $B < 1$, paramagnetic for $B > 1$ and undergoes a QPT at $B = 1$, where the system is in a critical phase. As expected, the properties of the system are very different in different phases.

For benchmarking, I will first study the complex network of mutual information, reconstructed with VQE and pairwise tomography, in different phases and compare them with ones in the paper of Valdez et al. [29]. Figure 10 shows the mutual information network with three different values of the magnetic field. In the ferromagnetic phase, the graph is dense, with most links strongly present. When approaching the critical value, the longest links start to fade out and, in the paramagnetic phase, only nearest-neighbour links are strong. These results match those
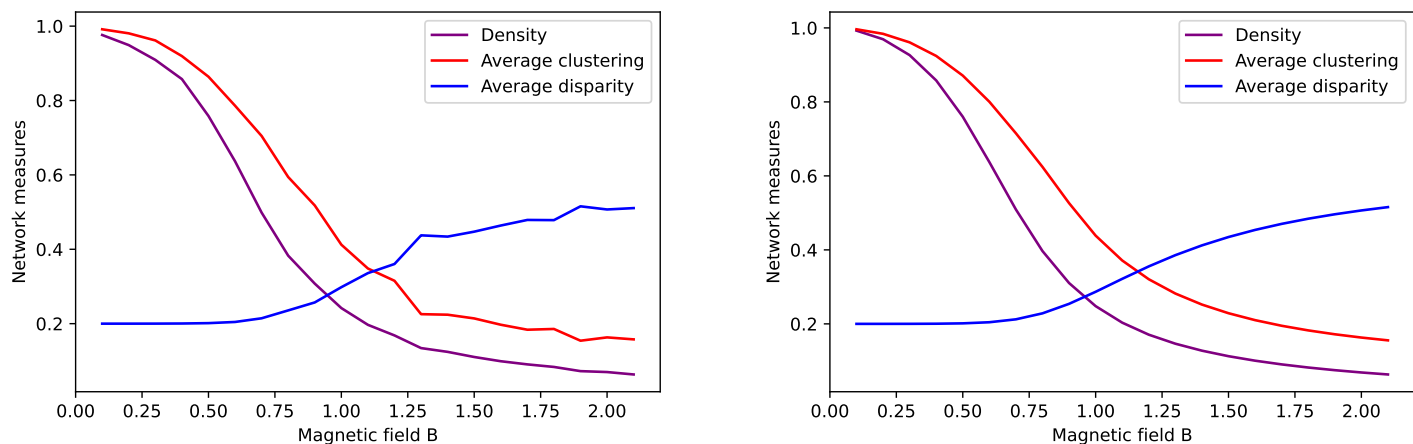
(a) VQE solution (b) Exact solution

Figure 11: Network measures of mutual information for the Ising model. The magnetic field is rescaled by J.

of Valdez et al. [29]

We can further analyze the mutual information network using different network measures. In Figure 11, the density, the average clustering and the average disparity are displayed for the Ising model with 6 qubits. Both exact diagonalization and VQE solutions are presented so one can see that aside from slight deviations they are same. The results also match those of Figure 10, as one can see that the density of the links and the average clustering drop as the magnetic field increases. The distribution of links is very homogeneous for low magnetic field values as one can see from the low average disparity. It then approaches the value of $1/2$ as the magnetic field increases and the links to nodes farther away fade out and links to nearest neighbors start to dominate. When comparing the results to those of Valdez et al., one can see that the density and average clustering have a good match when taking into consideration the difference in the system size. However, in their result, the average disparity approaches 1 as the magnetic field increases. As discussed before, the value of disparity of a node should be 1 only when one of the links connected to
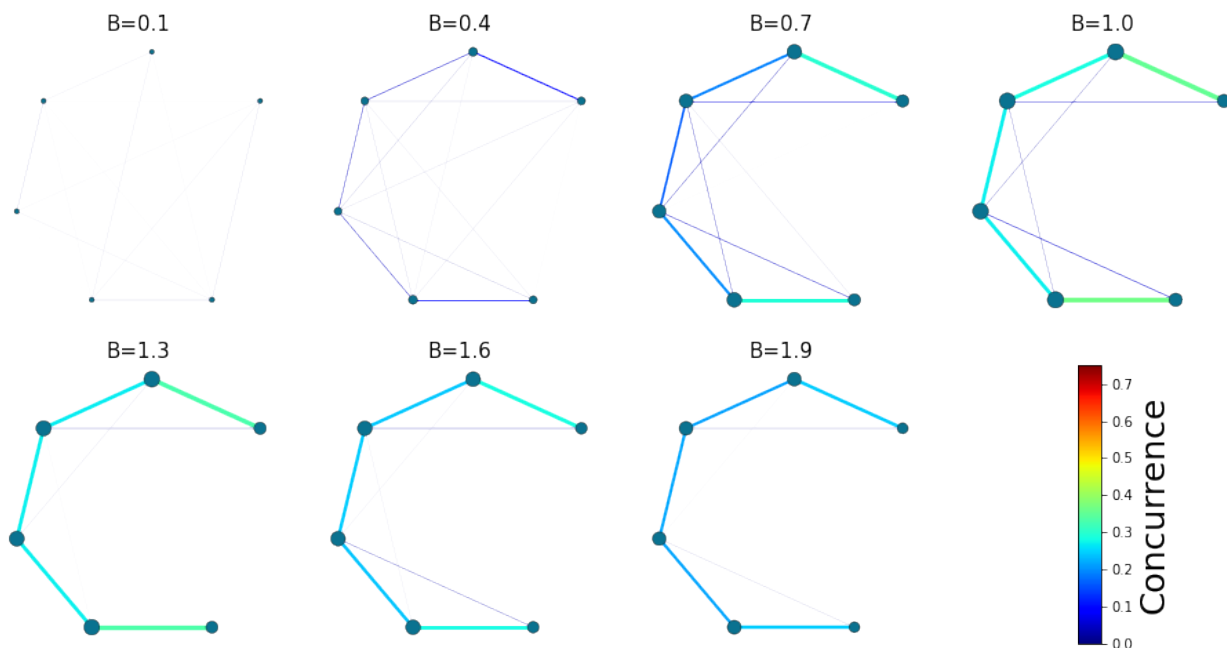
Figure 12: Concurrence networks of the Ising model for various magnetic field values. The magnetic field is rescaled by J.

the node dominates over the others. In our case, for $B = 2$, the mutual information graph is close to a nearest-neighbour chain, i.e., every node has similar links to both neighbors, left and right, and very low connection to every other node. Considering this, we can do a short calculation. If one approximates the links to farther away nodes to be zero and the links to nearest neighbors to be ω, we get the following value for the disparity of the node i:

$$Y_i = \frac{1}{s_i^2} \sum_{j=1}^{N} (\omega_{ij})^2 = \frac{2\omega^2}{(2\omega)^2} = \frac{1}{2}. \tag{35}$$

This result is consistent with Figure 11. Following this reasoning, I conclude that the results presented here are accurate.

The concurrence networks of the Ising model have not been studied before in the literature, so I will now present some new results. The concurrence networks
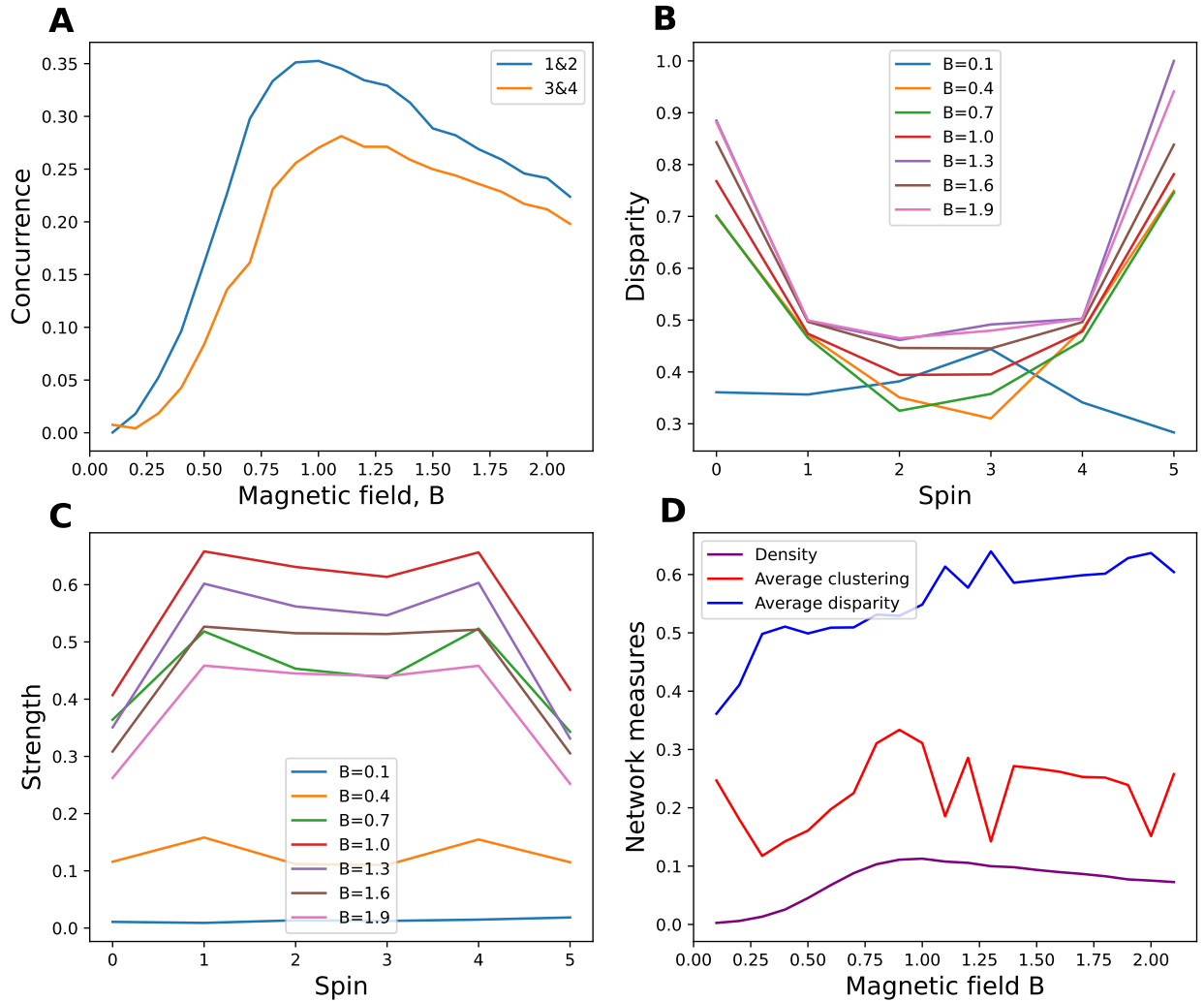
Figure 13: Analysis of the Ising model for 6 spins. A) Concurrence of edge spin pair, 1 and 2, and bulk spin pair, 3 and 4, as the magnetic field is varied. The spins are same as in figure 12, counting counter-clockwise and starting from upper rightmost spin. B) Disparity of each node for different values of B. C) Strength of each node for different values of B. D) Average network measures for varying magnetic field B.

for various magnetic field values are shown in Figure 12. Concurrence increases as the magnetic field grows and caps at the critical value $B = 1$ after which it starts to slightly decrease. In all cases, the concurrence of the edge pairs is higher than of the bulk. This can be seen more clearly in Figure 13A. The rate of change for both pairs is almost the same aside for low values of B, for which the concurrence of the edge pair increases faster. This behaviour is different from spin-1/2 XX chain as for it the order switches as the magnetic field is varied [36]. The results for low values of B (e.g $B = .01$ in Figure 12) are not reliable, because when there is low amount of entanglement, the fluctuations due to finite statistics are significant and can even lead to non-zero values even for separable states [11].

Other properties of the concurrence network of the Ising model are seen in figure 13. The disparities of each spin are shown in figure 13B. For all values of B the bulk of the chain is clearly more homogeneous while the edge spins present high disparity since their local connectivity is dominated by a single link. The disparity does not exhibit significant changes for different magnetic field values except for $B = 0.1$ when the aforementioned statistical fluctuations are large. In figure 13C one can see that the total strength is highest at the critical value $B = 1.0$. Also the edge spins have less strength than the bulk spins. In figure 13D it is seen that the density peaks just before the critical value but stays generally low as can be also been seen in the concurrence graphs of Figure 12. The average clustering fluctuates slightly and the average disparity slowly increases with the magnetic field. These fluctuations are most likely due to the limited number of shots used in the pairwise tomography. This would be reduced by increasing the number of shots, but it would also make the tomography more time consuming. The increase of average disparity is seen in the concurrence network as for lower values of B the network has few next-nearest links which fade out as B increases and the network becomes nearest neighbor dominant and heterogeneous.

2.1.3 The spin-1/2 XX model

Next the spin-1/2 XX model with the Hamiltonian given in Equation (15) will be explored. The system has been studied in papers of Son et al. [36], Sokolov et al. [9] and García-Pérez et al. [11] and the goal is to first reproduce these results and then present new ones. As explained in an earlier chapter, the ground state is characterized by sequence of N energy level crossing which happen at magnetic field values of $B_k = \cos[k\pi/(N+1)]$, with $1 \leq k < N$, for $0 < B < 1$. Models with exactly the magnetic field value of $B = B_k$ for some k have degenerate ground state, which leads to some arbitrariness in trying to find the ground state with VQE. To counter this, I will consider magnetic field values that lie in middle points of these energy level crossing. The considered values are therefore $B_k = (\cos[k\pi/(N+1)] + \cos[(k+1)\pi/(N+1)])/2$ for $k = \{1, \ldots N-1\}$.

Figure 14 shows the concurrence networks for these values of the magnetic field. One can easily see the changes in the network structure. These results match almost exactly the ones in the paper of García-Pérez et al.[11]. In that paper, they used the exact solution of the ground state of the XX model and then did pairwise tomography on it. Here, the ground state is found with VQE and the same pairwise tomography method is used. In the paper of Sokolov et al. [9] the structure of entanglement communities, i.e., groups of nodes with higher density of connections, were studied and they noted that the number of communities matches exactly the value of k in the magnetic field for $0 \leq B < 1$. The same phenomenon can be observed in Figure 14. One can also notice the change in the entanglement of edge spins versus bulk spins as was studied in the paper of Son et al. [36]. When B is near either 1 or -1, the bulk spins are stronger than the edge spins and when B approaches 0, the edge spins take over and display much higher concurrence. The scaling of concurrence for edge spin pair, 1 and 2, and for bulk spin pair, 4 and 5, for varying magnetic field is shown in figure 15A.
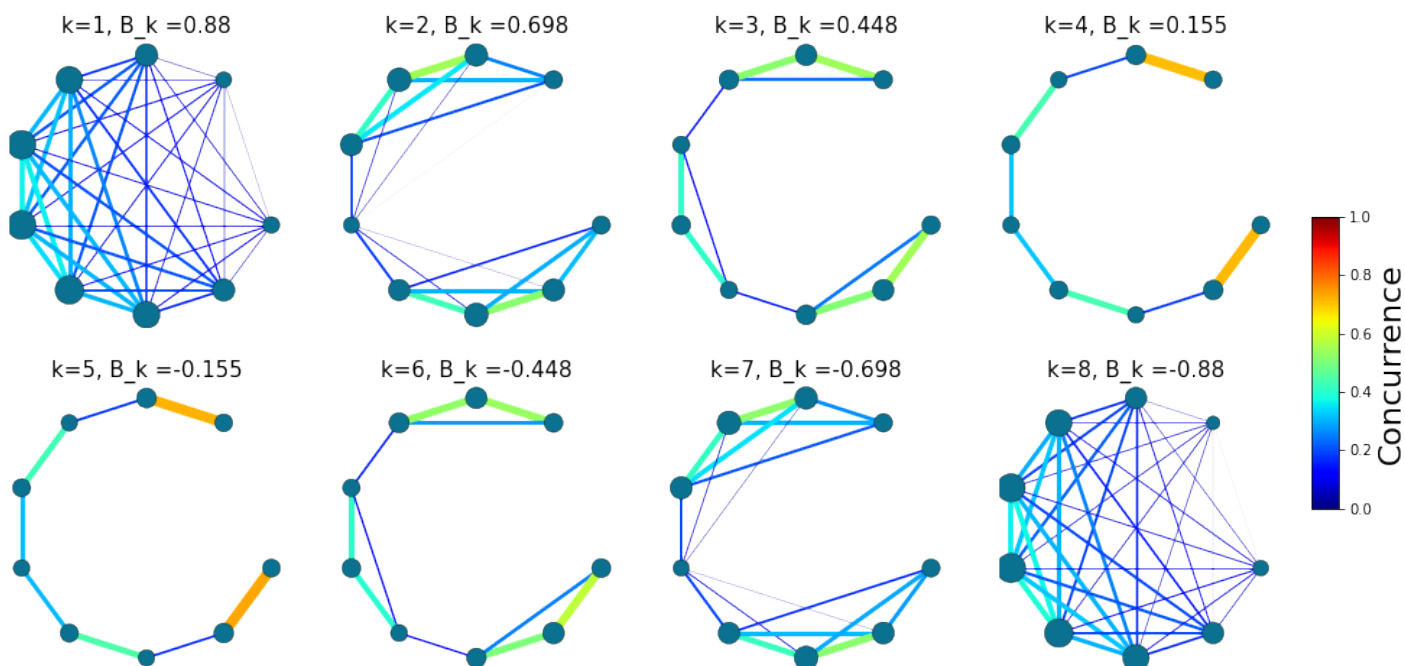
Figure 14: Concurrence networks of the spin-$1/2$ XX model for different B_k where $k = \{1, \ldots, 8\}$. The magnetic field is rescaled by J.

The disparity of each node is shown in figure 15B. When the magnetic field is close to values 1 or -1, the distribution of links is very homogeneous. At the same time, the bulk of the chain has much higher strength than the edges. Also, figure 14 shows that the graph is fully connected. Therefore, while the concurrence is distributed heterogeneously on the larger scale, as shown in the strength figure, the local heterogeneity is constant across the chain, as seen in the disparity figure. The same behaviour was noticed in the paper of Sokolov et al. and in it was explained that this behaviour indicates high symmetry close to the quantum phase transition [9]. Close to $B = 0$ the distribution changes into a more heterogeneous one.

The small size of the system restricts the comparison between the paper of Sokolov et al. of the peaks in the disparity figure 15B as there was discussed.
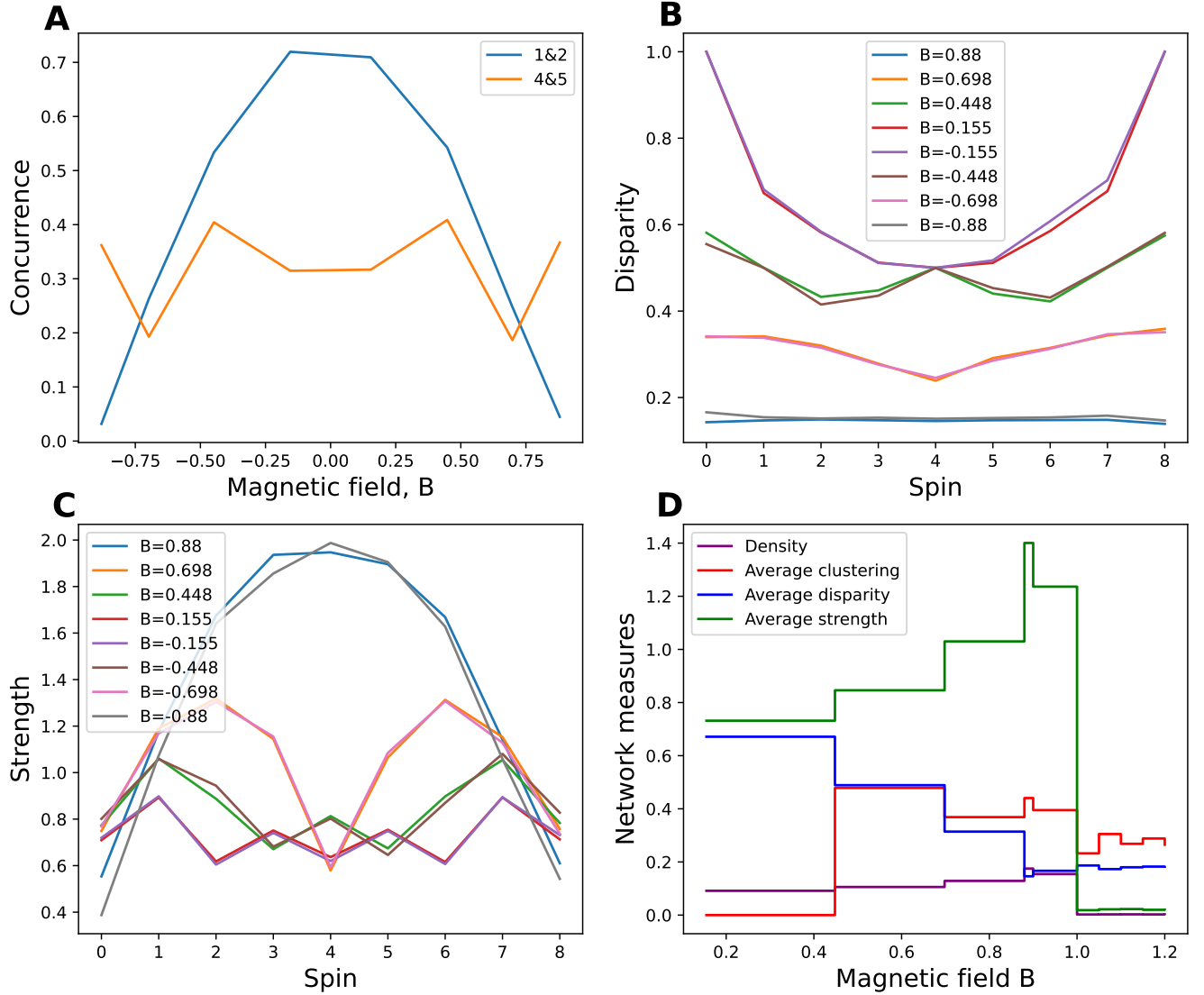
Figure 15: Analysis of the concurrence network of the spin-1/2 XX model for 9 spins. A) Concurrence of edge spin pair, 1 and 2, and bulk spin pair, 4 and 5, as the magnetic field is varied. The spins are same as in figure 14, counting counter-clockwise and starting from upper rightmost spin. B) Disparity of each node for different values of B. C) Strength of each node for different values of B. D) Average network measures for varying magnetic field B. The magnetic field is rescaled by J.

Still, it can be noted that the disparity of the edges increases compared to the bulk for values of $B < 0.5$. For low values of B, the system changes from long interactions to only nearest neighbor interactions, which causes the disparity of edge spins to become 1. The strength figure 15C displays similar properties as in the reference. The number of peaks matches the number k of the magnetic field which matches the number of detected communities in the system.

Average network properties of the system are shown in figure 15D for $0 < B < 1.2$. The quantum phase transition can be seen at $B = 1.0$ when the average strength and density drop close to zero. Some weak non-zero links still exists for $B > 1$ as seen from the average clustering and small average strength. In this region, the state is separable, so these fluctuations originate from the finite number of measurements for the tomography.

For completeness and as new results, the same analysis as done previously for concurrence is now done for mutual information. In Figure 16 the mutual information networks for different energy levels are shown. Same properties can be seen as in concurrence networks 14. In addition, new phenomena can be observed, because mutual information quantifies both classical and quantum correlations. Even though the system changes into nearest neighbor correlations for low values of B, classical correlations still persist as can be seen from the many non-zero links in the mutual information graphs. The community structure formations can still be observed, although not as strongly as in concurrence networks. However, the increase of entanglement for edge spins can clearly be seen. In figure 17A the of edge and bulk mutual information scaling is shown and the shape is very similar to the concurrence one.

Figure 17B shows the disparities of each spin for different values of the magnetic field and displays some of the properties as in concurrence: Disparity is low for B near 1 and -1 and it increases with magnetic field. The relative increase of edge
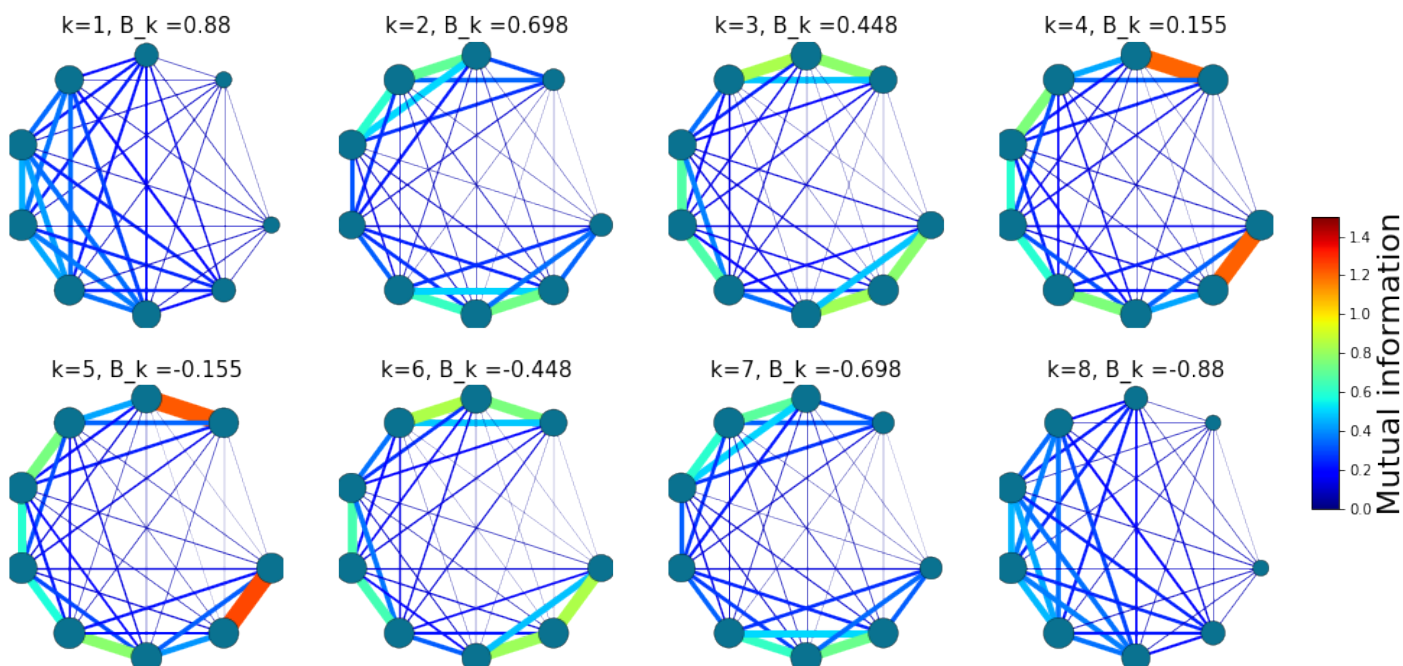
Figure 16: Mutual information networks of the spin-$1/2$ XX model for different B_k where $k = \{1, \ldots, 8\}$. The magnetic field is rescaled by J.

spin disparities is much stronger that in concurrence. For B near value 0, not only the spin closest to the edge but also the second most see increase in disparity unlike for concurrence where the spin nearest to the edge was much higher than the second one. Note that the absolute values for disparities are lower but the relative difference between two edge and bulk spins is higher. The increase of pairwise mutual information is much stronger than for concurrence which is why the second closest spin has heterogeneous distribution of links as the edge link dominates all others. Figure 17C also shows similar effects as with concurrence: The number of peaks matches the value of k although this is obscured for the values of B closest to zero. The difference is that as B decreases the total strength increases as can also been seen in figure 17D. The reverse happened for concurrence. Figure 17D also
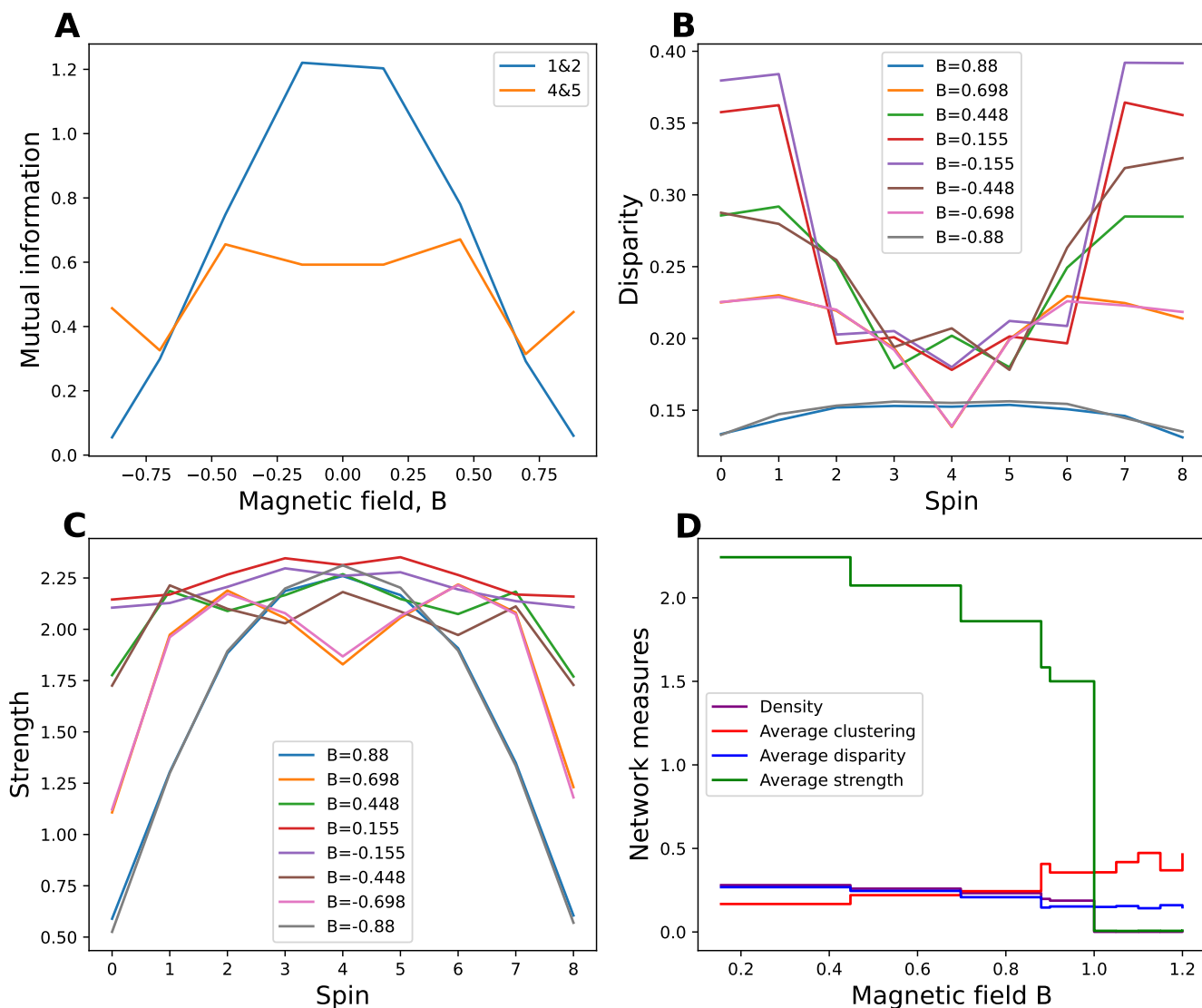
Figure 17: Analysis of the mutual information network of the spin-1/2 XX model for 9 spins. A) Mutual information of edge spin pair, 1 and 2, and bulk spin pair, 4 and 5, as the magnetic field is varied. The spins are same as in figure 16, counting counter-clockwise and starting from upper rightmost spin. B) Disparity of each node for different values of B. C) Strength of each node for different values of B. D) Average network measures for varying magnetic field B. The magnetic field is rescaled by J.
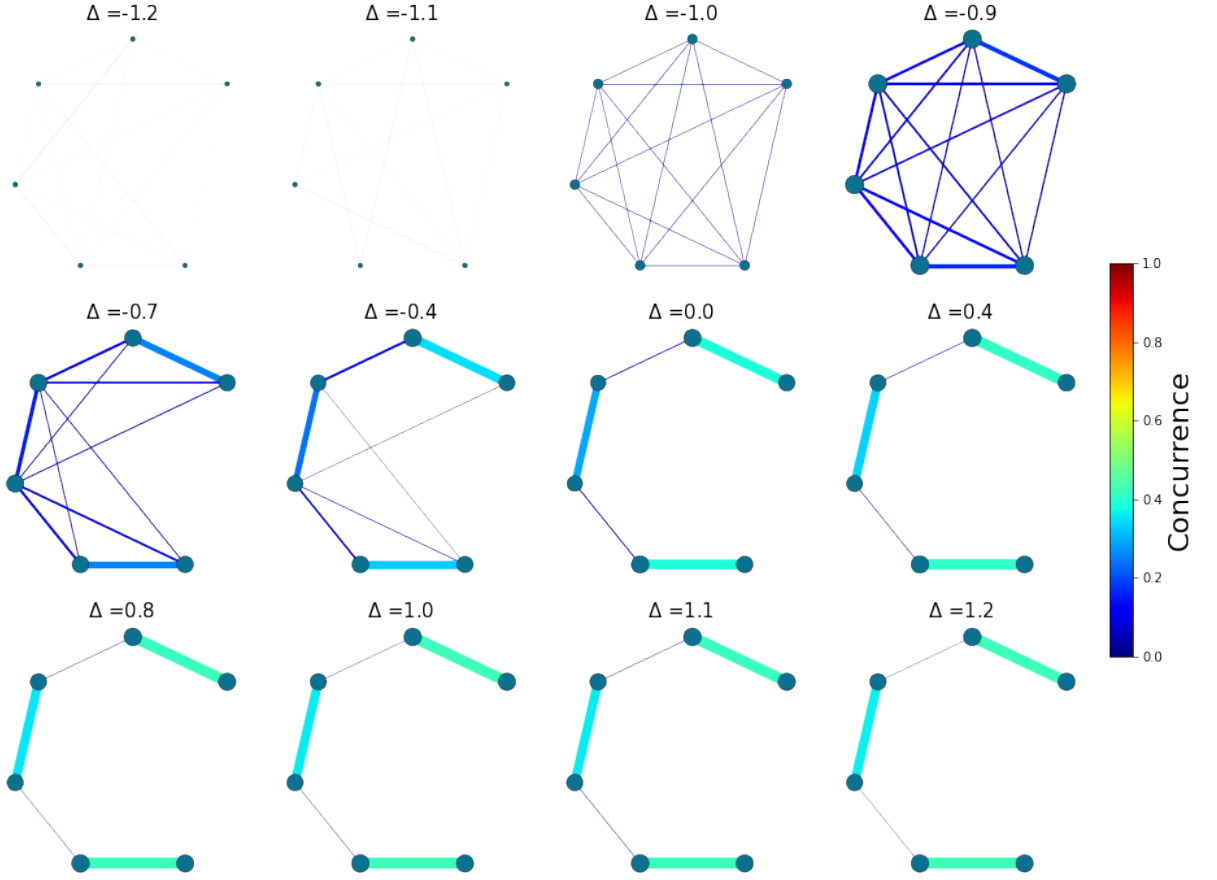
Figure 18: Concurrence networks of the XXZ model for 6 spins. The spin anisotropy is rescaled by J.

shows the same effect of the quantum phase transition at $B = 1.0$. The fluctuations originating from the finite amount of shots in the tomography can again be seen for $B > 1$.

2.1.4 The XXZ model

The XXZ model, with the Hamiltonian introduced in Equation (16), is the third example studied in this thesis. No previous studies of the pairwise correlation network
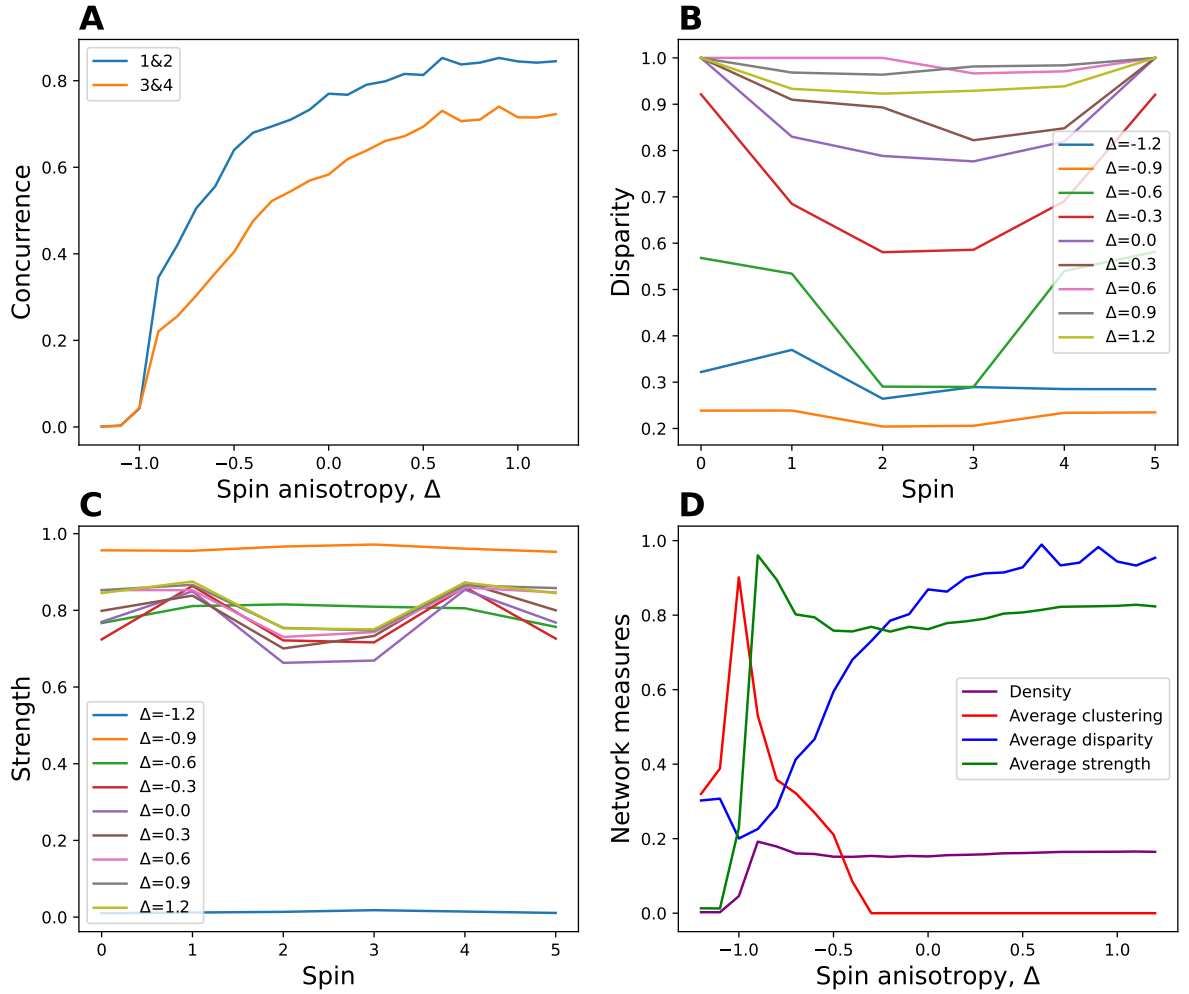
Figure 19: Analysis of the concurrence network of the XXZ model for 6 spins. A) Concurrence of edge spin pair, 1 and 2, and bulk spin pair, 3 and 4, as the spin anisotropy is varied. The spins are same as in figure 18, counting counter-clockwise and starting from upper rightmost spin. B) Disparity of each node for different values of B. C) Strength of each node for different values of B. D) Network measures for varying spin anisotropy Δ. The spin anisotropy is rescaled by J.

properties of XXZ model have been carried out before to the best of my knowledge, so all results presented here are novel. This section is a proof of concept on how
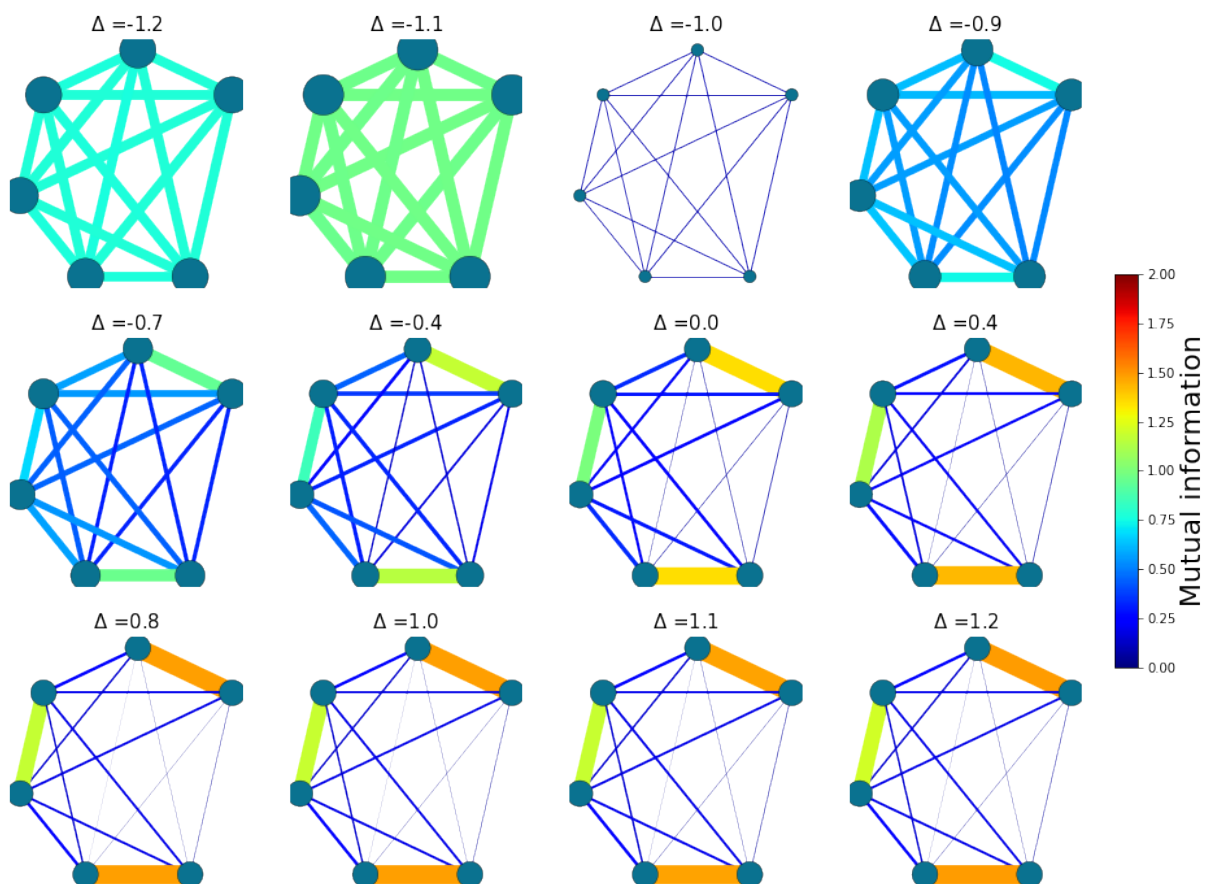
Figure 20: Mutual information networks of the XXZ model for 6 spins. The spin anisotropy is rescaled by J.

the method presented in this thesis can be used to study any quantum system with simulations rather than analytically.

I remind that the XXZ model is ferromagnetic for $\Delta < -1$ and anti-ferromagnetic for $\Delta > 1$. Both phases are also gapped. Between $-1 < \Delta < 1$, the system is critical.

The XXZ model does not have the same kind of symmetry for the spin anisotropy as the spin-1/2 XX had for magnetic field, as can be seen from the concurrence in Figure 18 and mutual information in Figure 20. For positive values of Δ the system
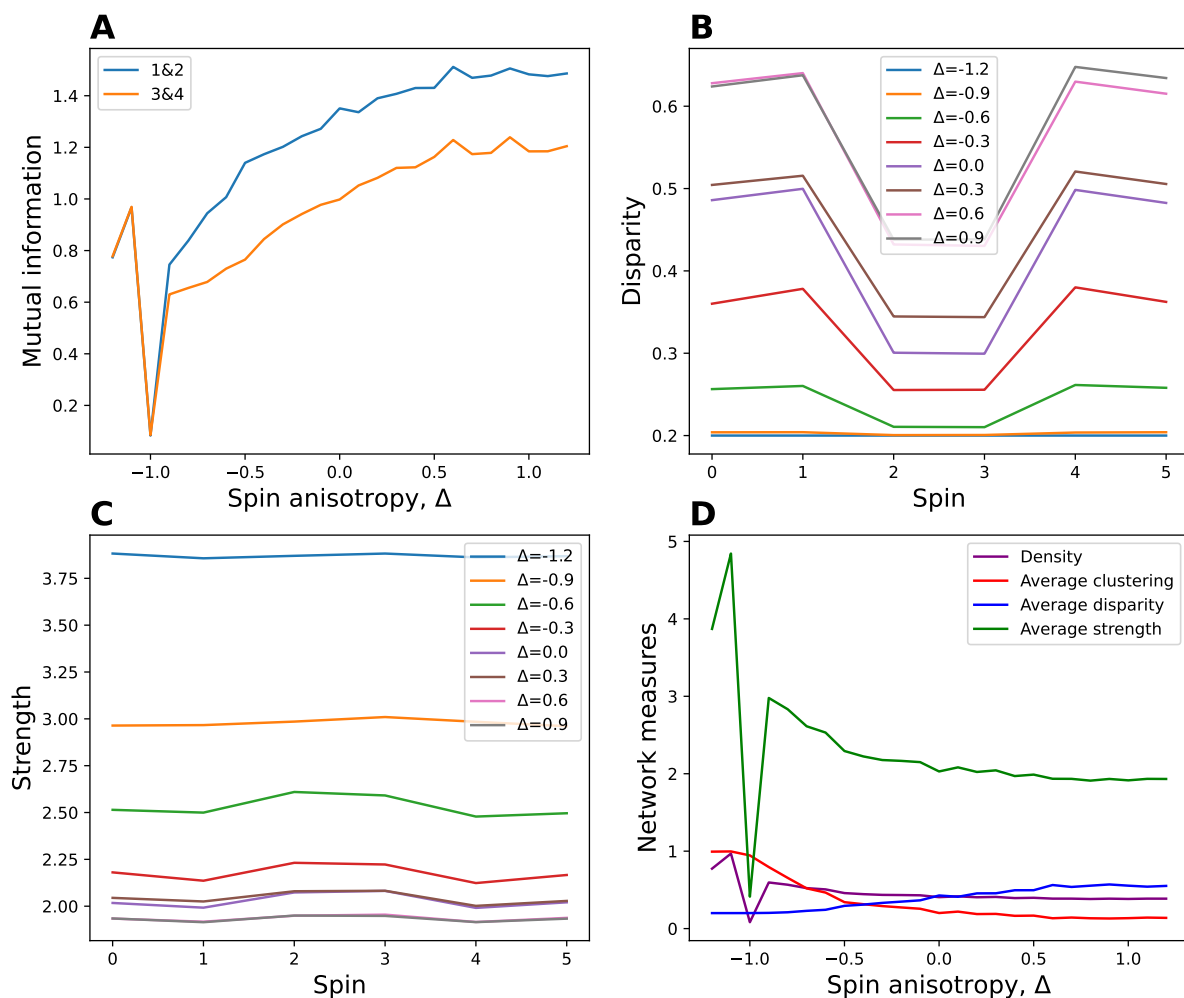
Figure 21: Analysis of the mutual information network of the XXZ model for 6 spins. A) Mutual information of edge spin pair, 1 and 2, and bulk spin pair, 3 and 4, as the spin anisotropy is varied. The spins are same as in figure 18, counting counter-clockwise and starting from upper rightmost spin. B) Disparity of each node for different values of B. C) Strength of each node for different values of B. D) Network measures for varying spin anisotropy Δ. The spin anisotropy is rescaled by J.

does not undergo any significant changes. For negative values the entanglement structure exhibits notable transformations. Below $\Delta < -1$ the system seems to be separable, because the small links seen in the Figure 18 are most likely due to statistical fluctuations. A change in the network happens at the QPT point at $\Delta = -1.0$. As the spin anisotropy increases to around $\Delta = -0.9$, the average strength of the concurrence network jumps to its highest point as seen in Figure 19D and the distribution is very homogeneous. As the spin anisotropy continues to increase, the strengths of concurrence links decrease slightly and the distribution changes to more heterogeneous one as the entanglement concentrates on three strong pairwise links. For $B > -0.5$ the edge pairs have slightly stronger entanglement than the middle pair as seen from the concurrence strengths in Figure 19C. The relative entanglement evens out when Δ increases. The effect is seen much more strongly in the mutual information disparities in Figure 21 and instead of fading as Δ increases, it becomes stronger. Although there is a QPT point at $B = 1.0$ no significant changes are visible in the results presented here. This might be due to the finite size of the system but is not explored further as it is beyond the scope of this work.

The phenomena for values $\Delta > -1$ are replicated in the mutual information networks in Figure 20 but one can also see the classical correlations even when no entanglement exists. Classical correlations are the strongest below $\Delta < -1$ as seen from the strong networks in 20 even though the concurrence graphs in 18 are very weak.

In Figures 19A and 21 the pairwise concurrence and pairwise mutual informations of spin 1 and 2 at the edge, and 3 and 4 at the bulk, are shown. They match at $\Delta \leq -1$ and above that, the edge pair initially becomes more entangled after which they scale similarly. In Figures 21C and 21D, the total strength of mutual information deceases as the spin anisotropy increases.

The ground state of the system was hardest to find for values is $\Delta = -1.0, -1.1$ and -1.2 because the ground state energy was degenerate. This could lead to some errors in the data for those values.

2.2   Emergent space from quantum entanglement

Quantum gravity has been long thought to be the missing piece in fundamental physics [44]. Finding the theory of quantum gravity has been very elusive despite the many different attempts, such as string theory and loop quantum gravity [45], [46]. The common approach has usually been to take an already existing theory and try to quantize it to make it work even in the smallest scales. An alternative approach, which has seen lots of research activity in the last decades, is to try find gravity in quantum mechanics itself. Gravity could be an emergent phenomenon of complex quantum systems. Approaches to study quantum gravity trough complex quantum network manifolds and emergent complex network geometry have been made [47, 48]. The tools introduced in this thesis can enable research in this area beyond purely analytical work. We have already seen how the methods can be used to extract information from the network entanglement structures of quantum may-body systems. By properly analyzing this information, I will study how geometry can emerge from entanglement.

Entanglement is a fundamental aspect of quantum mechanics and it constructs complex structures in quantum systems. It has been suggested that these structures could lead to emergent phenomena with relations to gravity and space[8]. Reasons to believe that quantum mechanics has connections to the geometry of space have emerged from holographic models and, more specifically, from the AdS/CFT corre-spondence [49]. A mapping between a $d+1$ -dimensional gravitational theory and a d-dimensional quantum field theory on the boundary was found by Juan Maldacena in 1997 [50]. The field has since evolved and it now combines many areas of physics

,such as quantum information and black hole thermodynamics. The same theory can also be used to reason that there is a connection between highly entangled particles and wormholes, the so-called EP=EPR conjecture [51], [52]. Commonly these phenomena are studied in the context of black holes, which makes it mostly theoretical research. However, this line of research is important in the study of fundamental physics, which motivates alternative approaches that can benefit from using quantum computers.

Here, we adopt the approach of Cao et al. [8]. First, few specific properties are checked that the systems need to fulfill to be applicable in this analysis. These will be explained below. Then, pairwise mutual information between parts of the system are used to construct a metric which tells how different parts of the Hilbert space are connected. This metric is then used to embed the system into a smooth manifold. Then the effect of entanglement perturbations on the state's geometry can be studied. Eventually, with the information obtained from theses studies, equations linking the energy of the state and its geometry, which are reminiscent of Einstein's equations, can be constructed. This procedure is general and can be done with any quantum systems which fulfill the requirements. Here, I will perform the procedure with the Ising model.

2.2.1 Entanglement area laws

One of the most interesting ideas from the holographic principle is the formula of the entropy of a black hole. Instead of scaling with volume, as one would expect, this idea suggests that the scaling is proportional to the area of the black hole instead. This has lead to advances in the study of quantum information in black holes and towards a possible solution to the so called *black hole information paradox* [53]. Any system with $GM > R/2$ (G is the gravitational constant, M is the mass of the system and R is the radius of the system) collapses into a black hole, the entropy of

a black hole has to be the upper bound for the entropy of any system in the space. This constraint is known as the holographic bound.[8]

A related interesting question is whether the Hilbert space describing a region of space is finite- or infinite-dimensional. According to quantum field theory, our most established and experimentally tested theory, a region of space has infinite degrees of freedom. As a consequence, the entropy of such region is also infinite because its infinite degrees of freedom are entangled with infinite degrees of freedom outside the region. But if the discussion above is considered, a finite part of space cannot have infinite entropy and therefore quantum field theory is not the final answer in physics. [54]

A possible solution to this problem is to assume that a physical theory giving full description of nature, including gravity, has to be a finite-dimensional factor of Hilbert space for any local region. If a region R of space is finite, we should be then able to decompose the Hilbert space of the whole space into parts $\mathcal{H}_{\mathrm{sys}} = \mathcal{H}_R \otimes \mathcal{H}_{\overline{R}}$, where $\overline{R}$ is the complement of the system. How many times the decomposition can be done depends on the system. For example, the Hilbert space of a spin chain can be decomposed all the way to the product of single-qubit Hilbert spaces, $\mathcal{H}_{\mathrm{spinchain}} = \bigotimes_{\mathrm{i}} \mathcal{H}_{\mathrm{i}}$. [54]

When studying entanglement phenomena, it is often more interesting to consider how the entanglement scales when the system size grows, rather than its detailed value. Before, I explained that black holes obey an area law for entanglement entropy and, interestingly, the same kind of scaling can be found in all kinds of systems, even in quantum spin chains. However, a typical quantum system picked at random will most likely obey a volume law as one can deduce by considering the expected entanglement entropy of a system divided in two parts, $I \subset L$ and $O = L/I$, each composed of d-dimensional constituents. One then finds for the unitarily invariant
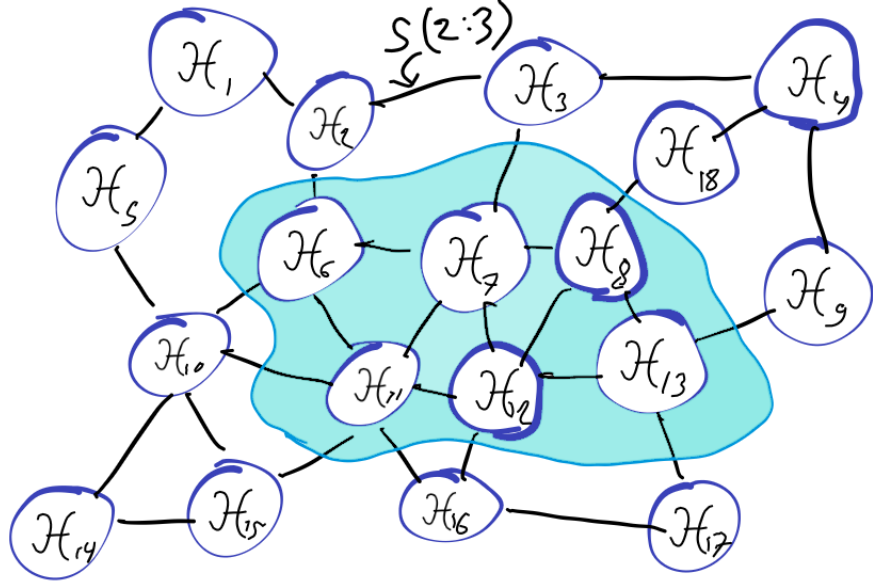
Figure 22: Graph where the nodes represent parts of the Hilbert space and links some interactions or correlations between them e.g. mutual information. Highlighted is a region of the system where its boundary consists of the links crossing the border. [8]

Haar measure

$$\mathbb{E}\left[S\left(\rho_I\right)\right] > |I| \log_2(d) - \frac{d^{|I|-|O|}}{2 \log_2(2)}. \tag{36}$$

Therefore, the typical entropy of a subsystem is asymptotically almost maximal and linear in the number of constituents $|I|$, which means that it follows a volume law. It is therefore intriguing to find that typical ground states usually follow an area law, sometimes with a small logarithmic correction. The entropy of a region in those systems is then linear in the boundary area of the region. [39]

In quantum many-body systems, this kind of behaviour arises from interactions that are typically local, i.e., subsystems interact mostly in short distance with nearest neighbors. Therefore, quantum correlations between a given region and its surroundings are established mainly trough its boundary. To visualize this, its helpful
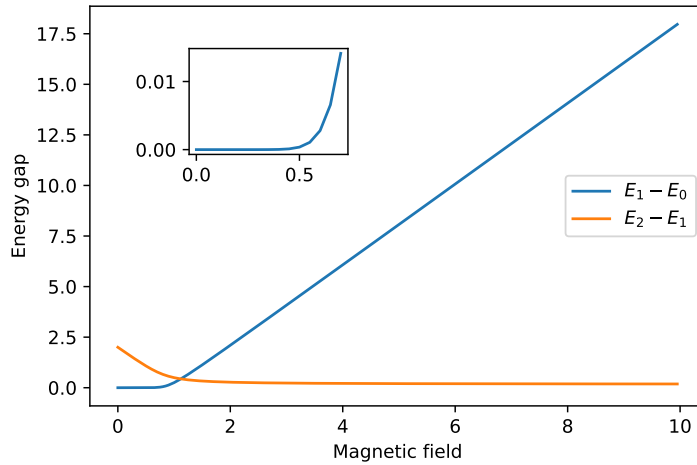
Figure 23: The energy gaps between the first eigenstate, E_0 and the second eigenstate, E_1, and the second eigenstate and the third eigenstate, E_2 of the Ising model for 12 spins. The energies and the magnetic field are rescaled by J.

to think of the system as a graph G of nodes L and links E, $G = (L, E)$, where the nodes represent subsystems of the Hilbert space and links the interactions or correlations between them, as in Figure 22. $1D$ spin chains can still be represented by $2D$ graphs, as correlations can go beyond the nearest neighbors, but for spin chains following an area law, the graphs will be approximately $1D$, and the boundary of a region is then just the 2 spins at its edges. Chains with periodic conditions will not have an edge. The area law then states that the entropy of a block $I = \{1, \ldots, n\}$ is then

$$S(\rho_I) = O(1), \tag{37}$$

where the big O notation describes the asymptotic growth rate of the function. In this case, it means that the entropy stays constant.

Quantum systems with local interactions and gapped Hamiltonians follow the area law [39, 55]. The ground states of quantum spin chains are usually gapped and local and therefore obey the area law behaviour [39]. In Figure 23, the energy gap

between the first and the second eigenvalues, and the second and third eigenvalues of the Ising model for 12 spins are shown. As the ground state of the system is degenerate for $B < 1$, the energy gap between the first two is expected to be almost zero and the gap between the ground state and the first excited state corresponds to the gap between the second and the third eigenstates. However, the energy gap between the first and second eigenstates is very close to zero only for values $B < 0.5$ after which the gap starts increasing, which is caused by the finite size of the system. When discussing area law, the gap between the ground state and the first excited state is considered. In Figure 24, the entropy of a subsystem is plotted as a function of its size for various magnetic field values. One can see that the area law is approximately followed by all values of B except for the critical phase $B = 1$. The area law is followed more accurately with values of B farther away from the critical value. Systems with $B = 1.5$ and $B = 2$ follow the area law quite accurately except when the size of the subsystem changes from 1 to 2 and from 10 to 11. The latter change originates from the finite size of the system, as the size of the subsystem becomes almost the same as the whole system.

The Hamiltonians for critical spin chains are gapless and therefore they do not strictly follow area laws but instead present a logarithmic scaling. They can be described by Conformal Field Theories (CFT), and the entanglement entropy is then

$$S(n) = \frac{c}{3}\log(n) + d, \tag{38}$$

where c is the central charge of the corresponding CFT and d is some non-universal constant. [32]

The following study will be conducted with states that obey area law. The discussion will first be general and will then move towards a specific use case, the Ising model, which has been noted to follow the area law accurately for magnetic field values $B > 1$. Consider again the graph representation for a system divided
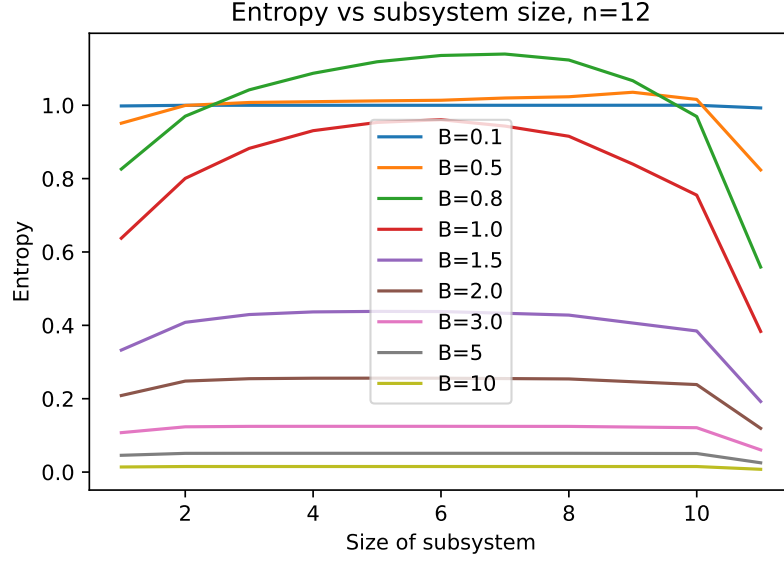
Figure 24: The scaling of entropy in 12 qubit Ising model for different magnetic field values. The entropy has been calculated for a subsystem taken from the middle of the spin chain by tracing others out. Chains with $B > 1$ approximately obey area law.

into sufficiently large regions A_p. We can calculate the entropy $S(A_p)$ of any region and the mutual information $I(A_p : A_q)$ between any two regions. A consequence of the area law is that we can use mutual information to calculate the entropy of any region. Consider a region $\mathbf{B}$ consisting of non-overlapping subregions A_p and the complement of this region $\overline{\mathbf{B}}$. We can then calculate the entropy of $\mathbf{B}$ by summing together all mutual informations crossing the boundary between $\mathbf{B}$ and $\overline{\mathbf{B}}$ as

$$S(\mathbf{B}) = \frac{1}{2} \sum_{p \in \mathbf{B}, q \in \overline{\mathbf{B}}} I(A_p : A_q). \tag{39}$$

In Figure 22, one would get the entropy of the shaded area by calculating the mutual information of the links crossing the cut line. This formula applies for most area law states, but the finite size of a system can affect. Even though the Ising model follows area law for $B < 1$, Figure 10 shows that it still exhibits long range correlations. Despite this, and for other systems which do not follow area law, Equation (39)

Spin	1	2	3	4	5	6	7	8	9	10	11	12
Error [%]	3.23	2.13	4.12	4.56	4.67	5.01	4.90	4.87	4.69	4.28	2.42	3.51

Table II: The relative differences of the entropy calculated by two different means for each qubit. The state is approximately redundancy-constrained.

can still be a good approximation. The states that obey this expression are called *redundancy-constrained.* [8]

In the paper of Cao et al. [8] they first considered general systems and then used a 1-dimensional antiferromagnetic Heisenberg chain as an example. However, instead of actually using mutual information in their analysis, they opted for estimating the mutual information by calculating the magnitude of the squared correlator in Equation (26) with Bessel functions [8]. The setup of this thesis allows for the entropy to actually be calculated through mutual information obtained from pairwise tomography. The quantum system that will be investigated is the 12-qubit Ising model with $B = 2$ as it was observed to obey the area law with decent accuracy. To make sure that the redundancy-constraint is fulfilled, the entropy of each qubit is calculated first by simply calculating the average of entropy obtained by tracing out the other qubits from every pairwise density matrix obtained from the pairwise tomography. Then, the mutual informations that are also obtained from the pairwise density matrices are used with Equation (39) to calculate the entropy. The relative differences for each qubit are shown in the table II. Small errors in redundancy-constrainedness are a consequence of the small size of the spin chain.

The total strength of a node which is the sum of the mutual informations of the links intersecting it, is upper bounded by the maximum entropy of the node as

$$S(A_p) = \sum_q I(A_p : A_q) \leq 2S_{\max}(A_p) \leq 2\ln(D_p), \tag{40}$$

where $D_p = \dim\mathcal{H}_{A_p}$ [8]. For a spin chain of qubits, the limit is then $S(A_p) \leq 2$.

2.2.2 Constructing the metric

Consider the mutual information graph of our quantum system. The goal is now to transform these mutual informations into distances between the nodes to construct a metric for the space. For a general graph $G(E, V)$, the transformation from information graph to distance graph is

$$G(V, E) = \tilde{G}(\tilde{V}, \tilde{E}), \tag{41}$$

which might be a non-trivial transformation. One easy simplifying assumption to make is to keep the vertices and edges fixed so that only the weights of the edges change. It is reasonable to assume that mutual information is higher between nearby parts of space and lower for distant ones. However, this is not always true as maximally entangled particles can be at arbitrarily distances from each other. One can think of this construction as being a new kind of notion for what is close and what is not. Even though entangled particles may not transfer information instantly to arbitrary distances, they are still strongly correlated. This kind of idea is known as the EP=EPR conjecture that will be discussed later. [8]

Now the distance graph's weights are defined as

$$w(p, q) = \begin{cases} \ell_{\mathrm{RC}} \Phi \left(I \left(A_p : A_q \right) / I_0 \right) & (p \neq q) \\ 0 & (p = q) \end{cases} \tag{42}$$

where ℓ_{RC} is the redundancy-constraint scale, Φ is some function and I_0 is for normalization. I set $\ell_{\mathrm{RC}} = 1$ without loss of generality. Also, if $I(A_p : A_q) = 0$ no edge is drawn. The normalization is chosen such that $I \left(A_p : A_q \right) / I_0 = 1$ for a maximally entangled state. This is the same as the limit for the entropy in Equation (40), so $I_0 = 2$.

The function Φ is generally determined by the system, but it has to fulfill some basic properties. The argument of the function is 1 for maximally entangled states, which are assumed to be close, so the first requirement is that $\Phi(1) = 0$. Unentangled

states are far apart from each other, so the second requirement is that $\lim_{x \to 0} \Phi(x) = \infty$. Also, Φ has to be non-negative and monotonically decreasing. For our simple system, $\Phi(x) = -\ln(x)$ will be suitable. [8]

These weights could be readily used to setup the metric. However, for vertices that are connected by multiple paths, the shortest one needs to be chosen. Let P be any path connecting two nodes p and q, and denote the path of vertices as $P = (p = p_0, p_1, p_2, \dots, p_k = q)$. The metric $\tilde{d}(p, q)$ is then constructed by choosing the shortest path between any two pairs as

$$\tilde{d}(p, q) = \min_P \left\{ \sum_{n=0}^{k-1} w(p_n, p_{n+1}) \right\}. \tag{43}$$

By construction, this metric satisfies the requirements for metric space: 1) $\tilde{d}(p, q) = \tilde{d}(q, p)$, 2) $\tilde{d}(p, q) = 0$ for $p = q$ and 3) $\tilde{d}(p, q) \leq \tilde{d}(p, s) + \tilde{d}(s, q)$, for any $s \in G$.

2.2.3 Classical multi-dimensional scaling

To construct the emergent space from quantum entanglement, we need tools to embed the metric obtained from mutual information to a smooth manifold. One approach is Regge calculus, which was originally crafted to study Einstein's general relativity in discrete space and it contains tools to construct a manifold from distances between vertices [56]. The approach used in this thesis is a method from classical data analysis called Multi-Dimensional Scaling (MDS). With it we can embed the metric into a symmetric manifold. The embeddings will be done to Euclidean $\mathbb{R}^D$ manifolds, and later perturbations to this manifold are considered. The embedding is isometric i.e. a distance-preserving transformation for flat geometries and a good approximation for spaces with small distortion. The goal is to find an embedding with the smallest dimension D which is still approximately isometric. Some distortion can arise from the arbitrarily chosen function Φ. [8]

Next I will describe the procedure to obtain a coordinate matrix $\mathbf{X}$ embedded in a D-dimensional space. The input will be the metric $\tilde{d}(p, q)$ for N vertices and

the output an $N \times D$ matrix $\mathbf{X}$, where the n-th row contains the D coordinate values of the n-th vertex in $\mathbb{R}^D$. First, define a new matrix $\mathbf{B}$ which is related to the coordinate matrix by $\mathbf{B} = \mathbf{X}\mathbf{X}^{\mathbf{t}} = (\mathbf{X}\mathbf{O})(\mathbf{X}\mathbf{O})^{\mathbf{t}}$, where $\mathbf{O}$ can be some arbitrary orthonormal transformation. The metric can be then related to the matrix $\mathbf{B}$ through the coordinates as follows [8]

$$\tilde{d}(p,q)^2 = \sum_{r=1}^{d} (X_{pr} - X_{qr})^2 \tag{44}$$

$$= \sum_{r=1}^{d} [X_{pr}X_{pr} + X_{qr}X_{qr} - 2X_{pr}X_{qr}] \tag{45}$$

$$= B_{pp} + B_{qq} - 2B_{pq}. \tag{46}$$

An unique solution is obtained by setting a constrain to center the embedding at the origin

$$\sum_{p=1}^{N} X_{pr} = 0, \quad \forall r. \tag{47}$$

From this follows that $\sum_{q=1}^{N} B_{pq} = 0$ and then we finally get the equation to construct the $\mathbf{B}$ matrix

$$B_{pq} = -\frac{1}{2}\left(\tilde{d}(p,q)^2 - \frac{1}{N}\sum_{l=1}^{N}\tilde{d}(p,l)^2 - \frac{1}{N}\sum_{l=1}^{N}\tilde{d}(l,q)^2 + \frac{1}{N^2}\sum_{l,m=1}^{N}\tilde{d}(l,m)^2\right). \tag{48}$$

To obtain the coordinate matrix $\mathbf{X}$ we just need to diagonalize $\mathbf{B}$ as $\mathbf{B} = \mathbf{V}\mathbf{\Lambda}\mathbf{V}^{\mathbf{t}}$, calculate its eigenvalues $\lambda_1 \geq \lambda_2 \geq \ldots \geq \lambda_N$, and choose the D non-zero eigenvalues and corresponding eigenvectors to construct the solution

$$X = (\sqrt{\lambda_1}\mathbf{v_1}, \ldots, \sqrt{\lambda_D}\mathbf{v_D}). \tag{49}$$

This is an isometric embedding of N points to a D dimensional Euclidean space and, if we wish to obtain an embedding into a lower dimensional space, we can choose
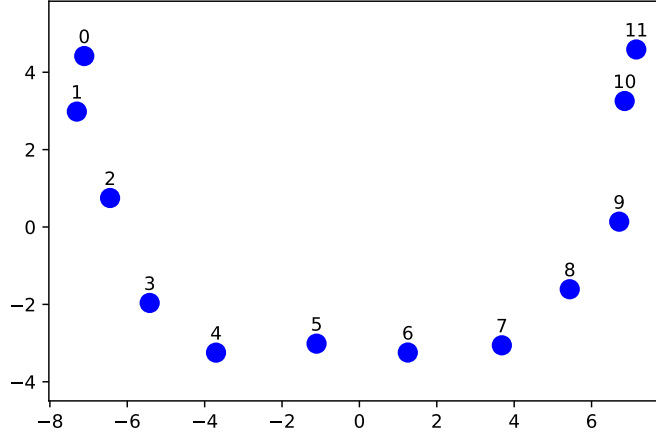
Figure 25: The embedding from multidimensional scaling for the Ising model with 12 spins and $B = 2.0$. The magnetic field is rescaled by J.

the D eigenvectors the highest eigenvalues. The error of the embedding will then be

$$\epsilon_D = 1 - \frac{\sum_{i=1}^{D} |\lambda_i|}{\sum_{i=1}^{N} |\lambda_i|}. \tag{50}$$

2.2.4 Embedding the Ising model to a manifold

The procedure described above will now be applied to the Ising model of 12 spins with magnetic field value of $B = 2$. VQE is used to find the ground state of the model and pairwise tomography is then used to extract the mutual information network from it. The redundancy-constrainedness of the state was already explored in the table II. Using Equations (42) and (43), the weights and the corresponding distance metric were calculated. Then, classical MDS was applied by using Equation (48) to calculate the $\mathbf{B}$ matrix, and from that the coordinate matrix $\mathbf{X}$. The resulting embedding to 2-dimensional Euclidean space can be seen in Figure 25. One can see that the spin chain is reconstructed with great accuracy, although the edges bend
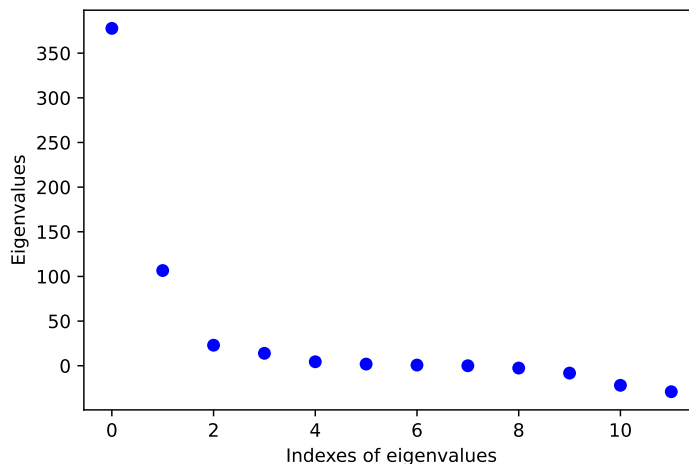
Figure 26: The eigenvalues of the **B** matrix of the embedding of the Ising model.

Dimensions of embedding	1	2	3
Error of the embedding, ϵ [%]	35.99	17.93	14.04

Table III: The errors in 1,2 and 3 -dimensional embeddings of the Ising model to an Euclidean manifold.

slightly. Slight bending happens due to the finite size effect, but the reason is mostly in errors coming from the methods. The errors are due to three things: 1) The state is only approximately redundancy-constrained, 2) the VQE result is good but not exact and 3) the pairwise tomography results in small errors due to finite statistical sampling. The resulting error is not large, but the MDS procedure seems to be sensitive to small changes in edge weights.

The eigenvalues of the B matrix are shown in figure 26. The first eigenvalue is much higher than the rest so the embedding is mostly 1-dimensional. However, the second eigenvalue is also quite high, so much better embedding is achieved onto a 2-dimensional manifold. The errors for 1,2 and 3 -dimensional embeddings can be seen in the table III.

2.2.5 Perturbations

VQE gives us the ground state of a system and now we will consider perturbations away from it and how it affects the MDS embedding and the emerging space. This line of research was proposed and shortly explored in the paper of Cao et al. to understand the relationship between entanglement and curvature of space[8]. The work was purely theoretical and with some assumptions on the quantum state, so no direct correspondence were stated. The following discussion is more hypothetical in nature, but it illustrates a use case for the method of the thesis.

For the perturbation, I have chosen the controlled $R_y(\theta)$-gate between two qubits, where qubit 2 is the control and qubit 9 is the target. The gate is added after the parametrized circuit that represents the ground state of the Ising model. The parameter of the gate is varied from 0 to 2π. The idea behind this numerical experiment is to study the EP=EPR conjecture, which states that the entanglement between two systems is, in some sense, analogous to a quantum wormhole. Two entangled particles can affect each others' quantum state through arbitrary distances, so in the language of our theory of emergent space, they can be considered to be close to each other. The effects of the perturbation are shown in Figure 27 for various values of θ. One can see that the spins 2 and 9 start closing on each other and eventually almost overlap. One needs to keep in mind that the embeddings are an approximation and there is ambiguousness in the interpretation.

Figure 28 quantifies the effects of the perturbation. The sum of pairwise mutual information of the whole system increases from the perturbation and one can see that the maximum of the perturbation happens at about $\theta = \pi$. The perturbation increases the mutual information of spins 2 and 9, the control and the target which corresponds to the spins closing on each other as seen in the Figure 27. Interestingly, the mutual information of the control spin, 2, and its neighbor, 1, and also of the target spin, 9, and its neighbor, 8, decrease as the perturbation grows. In addition,
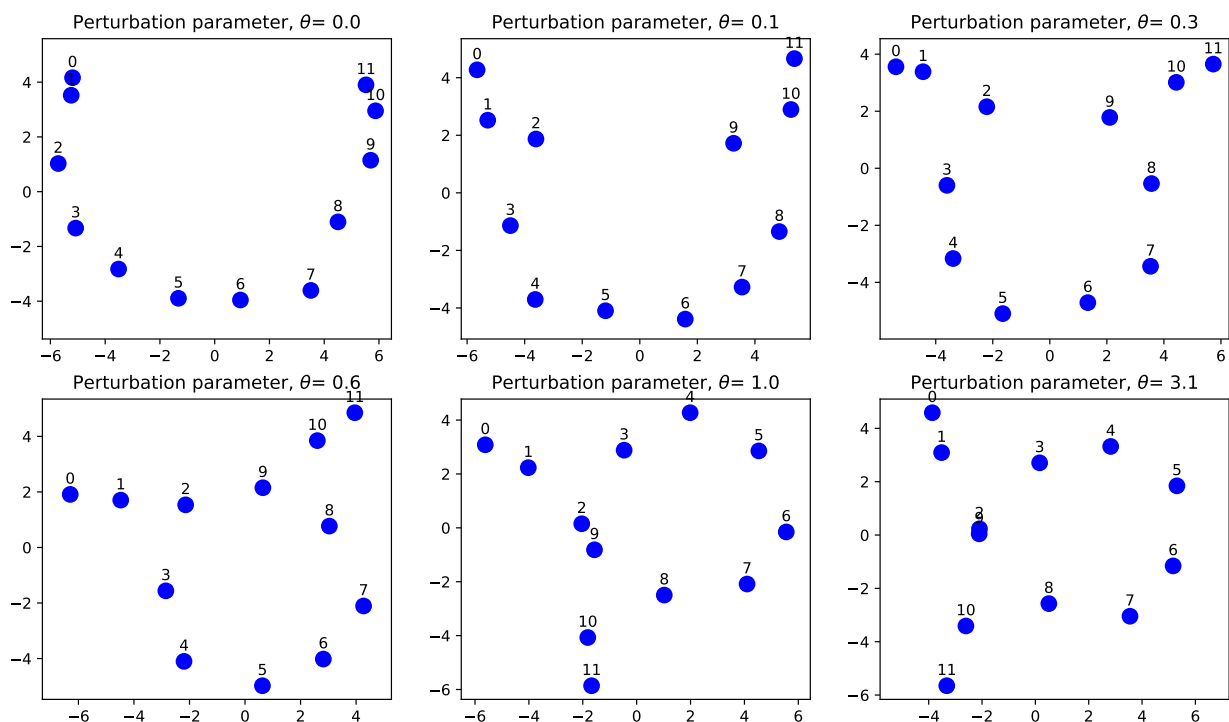
Figure 27: The MDS embedding in 2D of the Ising model which has been perturbed by a control-$R_y(\theta)$-gate where qubit 2 is the control and 9 is the target. The figures show the effect of the perturbation for different values of θ.

the mutual information of the control, 2, and the targets neighbor, 9, grows with the perturbation and same with the target, 9, and controls neighbor, 1. This behaviour was predicted in the paper of Cao et al. for two spins that become increasingly entangled with each other. This effect can be interpreted as a quantum proto-wormhole. It has no smooth classical geometrical presentation so the embeddings shown in figure 27 are not completely accurate, but partly capture the effects on the geometry. The embedding error is also plotted in the bottom of the Figure 28, and one can see that as soon as the perturbation starts, the 1-dimensional embedding error quickly increases. The 2 and 3-dimensional embedding errors also increase slightly. It is clear that no smooth Euclidean embedding exists even in 3 dimensions

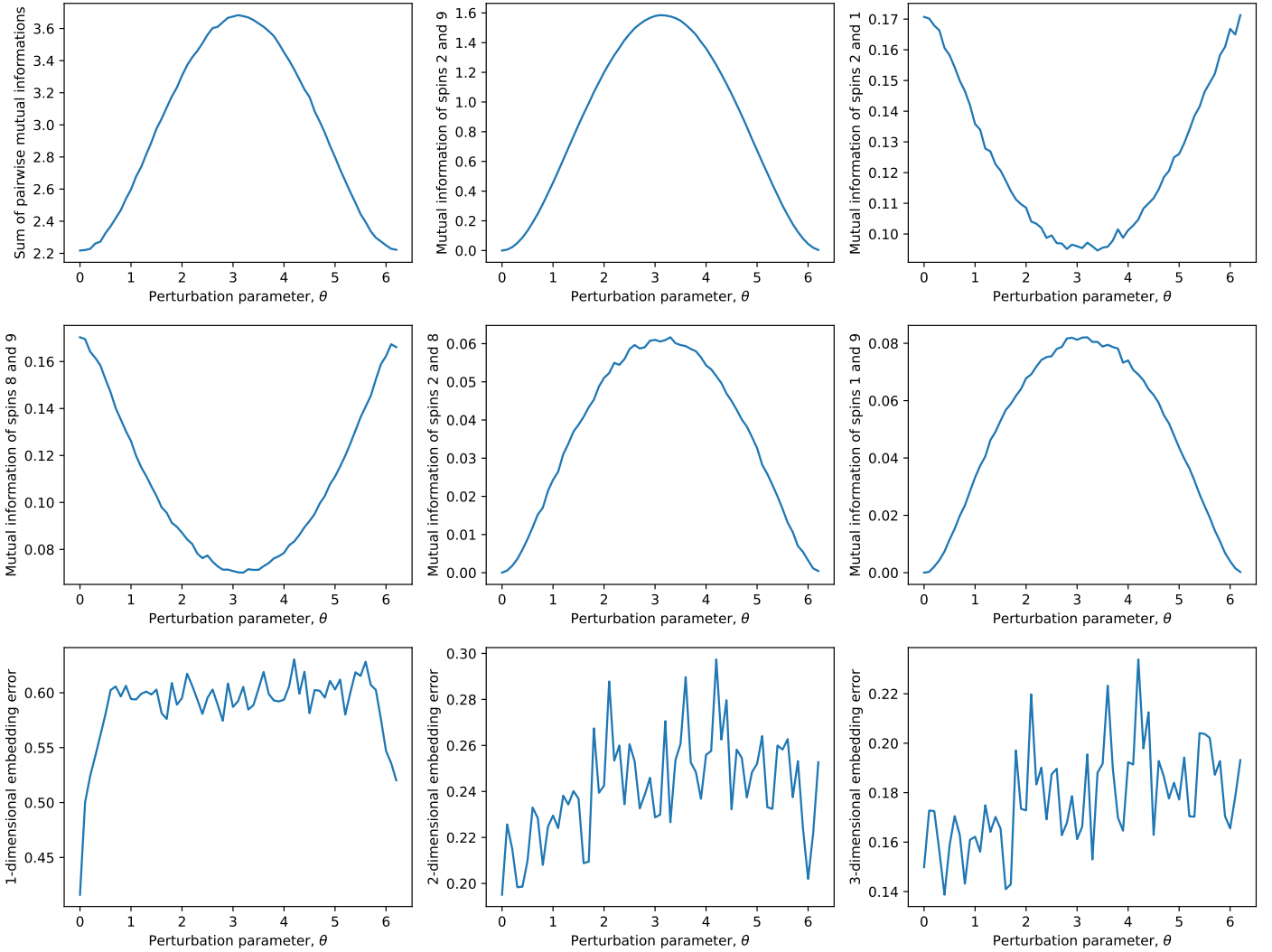Figure 28: Effects of the perturbation on the Ising model. A control-$R_y(\theta)$-gate was applied so that spin 2 was the control and 9 was the target. In each figure the x-axis represents the parameter θ which was varied from 0 to 2π.

for a highly perturbed system. Finding a connection between the entanglement perturbations and Einstein's equations of general relativity was also considered in the paper of Cao et al [8], which will be investigated in future work.

3 Conclusions

The main focus of this thesis has been to introduce a methodology to explore quantum entanglement phenomena on near term quantum computers. This methodology combines two existing quantum algorithms, VQE and pairwise tomography, which were first introduced, and then used, as a proof of concept, in two different case studies. An important aspect of the methodology is that it does not need a fault-tolerant quantum computer with millions of qubits, as those are still far in the future. Instead, the methodology can be used right now for small systems, and in the near future, for intermediate sized systems, which can already represent problems that can benefit from quantum advantage.

In this thesis, the simplest form of the VQE algorithm was used. Despite this, it efficiently worked with the studied examples. For more complex systems some advancements might be needed of which many examples already exist. Adapt-VQE changes the ansatz such that it is iteratively built from a set of building blocks to better suit the problem under study [57]. In the paper of García-Pérez et al., a method is introduced to optimize the measurement part of the VQE algorithm on-the-fly to increase the rate of convergence [26]. The same method can also be used to construct quantum state tomography, which could replace the pairwise tomography used in this thesis.

Pairwise mutual information and concurrence were proven to be good quantifiers of entanglement structures. They are complementary: concurrence provides information about the purely entanglement phenomena and mutual information considers both classical and quantum correlations. Together they give information about entanglement community structures, quantum phase transitions and network properties of the system.

Two study cases were considered as a proof of concept to benchmark the methodology, and also to study the problems themselves. First, the entanglement network

structures of quantum many-body systems was studied. Many results of the papers of Sokolov et al. [9], Valdez et al. [29] and Son et al. [36] were reproduced and also new results were presented. The systems under study were simple quantum spin chains, because 1) they did not require more advanced versions of the algorithms given their simplicity, 2) they are extensively studied in the literature, which is good for benchmarking, and 3) despite their simplicity, they still presented interesting properties that are not well understood without studying their emergent properties.

The methodology can also be used in the research of fundamental physics, which was proven by studying topics in quantum gravity, and more specifically, emergent space from quantum entanglement. The entropy distribution of a state fulfilling the area law and redundancy-constraints can be calculated from pairwise mutual informations, which was done using the ground state of the Ising model. This information was used to construct a metric that was embedded into a $\mathbb{R}^D$ Euclidean space using classical multi-dimensional scaling. Also, the effect of entanglement perturbations on the emerging geometry was explored.

All experiments for this thesis were performed on classical simulators, because of computation and time constraints. Also, with the current quantum computers provided by IBM that are accessed through the cloud, one would need to submit a separate job of quantum circuit simulation for each iteration in the VQE algorithm, which would slow down the process. In the future, it may be possible to submit the entire process of the algorithm at once, eliminating this limitation. In general, advancements in quantum technologies will enable more efficient usage of the methodology presented here, maybe to achieve quantum advantage for real world applications in the near future.

References

[1] P. Benioff, Journal of Statistical Physics **22**, 563 (1980).

[2] Y. Manin, *Computable and Uncomputable (in Russian)* (Sovetskoye Radio Moscow, 1980).

[3] R. P. Feynman, International Journal of Theoretical Physics **21**, 467 (1982).

[4] P. Shor, in *2013 IEEE 54th Annual Symposium on Foundations of Computer Science* (IEEE Computer Society Los Alamitos, CA, USA, 1994), pp. 124–134.

[5] J. Preskill, Quantum **2**, 79 (2018).

[6] Y. Cao, J. Romero, and A. Aspuru-Guzik, IBM Journal of Research and Development **62**, 6 (2018).

[7] E. Lucero, Unveiling our new Quantum AI campus, https://blog.google/technology/ai/unveiling-our-new-quantum-ai-campus/.

[8] C. Cao, S. M. Carroll, and S. Michalakis, Physical Review D **95**, 024031 (2017).

[9] B. Sokolov, M. A. Rossi, G. García-Pérez, and S. Maniscalco, arXiv preprint arXiv:2007.06989 (2020).

[10] J. R. McClean, J. Romero, R. Babbush, and A. Aspuru-Guzik, New Journal of Physics **18**, 023023 (2016).

[11] G. García-Pérez *et al.*, Physical Review Research **2**, 023393 (2020).

[12] R. Orús, Annals of Physics **349**, 117 (2014).

[13] K. Bharti *et al.*, arXiv preprint arXiv:2101.08448 (2021).

[14] C. Gidney and M. Ekerå, Quantum **5**, 433 (2021).

[15] IBM Quantum. https://quantum-computing.ibm.com/, 2021.

[16] R. Barends *et al.*, Nature **508**, 500–503 (2014).

[17] M. A. Nielsen and I. L. Chuang, *Quantum Computation and Quantum Information: 10th Anniversary Edition*, 10th ed. (Cambridge University Press USA, 2011).

[18] H. Abraham *et al.*, Qiskit: An Open-source Framework for Quantum Computing, 2019.

[19] A. Y. Kitaev, Russian Mathematical Surveys **52**, 1191 (1997).

[20] F. Arute *et al.*, Nature **574**, 505 (2019).

[21] H.-S. Zhong *et al.*, Science **370**, 1460 (2020).

[22] J. Preskill, arXiv preprint arXiv:1203.5813 (2012).

[23] M. Cerezo *et al.*, arXiv preprint arXiv:2012.09265 (2020).

[24] A. Peruzzo *et al.*, Nature communications **5**, 1 (2014).

[25] A. Asfaw *et al.*, Learn Quantum Computation Using Qiskit, http://community.qiskit.org/textbook, 2020.

[26] G. García-Pérez *et al.*, arXiv preprint arXiv:2104.00569 (2021).

[27] A. Kandala *et al.*, Nature **549**, 242–246 (2017).

[28] Y. Cao *et al.*, Chemical Reviews **119**, 10856–10915 (2019).

[29] M. A. Valdez, D. Jaschke, D. L. Vargas, and L. D. Carr, Physical review letters **119**, 225301 (2017).

[30] L. Bozanic, The Variational Quantum Eigensolver, https://medium.com/@lana.bozanic/the-variational-quantum-eigensolver-efb8fab14c85.

[31] J. Romero *et al.*, Quantum Science and Technology **4**, 014008 (2018).

[32] C. Bravo-Prieto, J. Lumbreras-Zarapico, L. Tagliacozzo, and J. I. Latorre, Quantum **4**, 272 (2020).

[33] J. R. McClean *et al.*, Nature communications **9**, 1 (2018).

[34] D. P. Kingma and J. Ba, arXiv preprint arXiv:1412.6980 (2014).

[35] J. Spall, IEEE Transactions on Automatic Control **37**, 332 (1992).

[36] W. Son, L. Amico, F. Plastina, and V. Vedral, Physical Review A **79**, 022302 (2009).

[37] C. Holzhey, F. Larsen, and F. Wilczek, Nuclear Physics B **424**, 443 (1994).

[38] P. Calabrese and J. Cardy, Journal of Statistical Mechanics: Theory and Experiment **2004**, P06002 (2004).

[39] J. Eisert, M. Cramer, and M. B. Plenio, Reviews of Modern Physics **82**, 277–306 (2010).

[40] S. Hill and W. K. Wootters, Physical Review Letters **78**, 5022–5025 (1997).

[41] W. K. Wootters, Physical Review Letters **80**, 2245–2248 (1998).

[42] U. Schollwöck, Annals of Physics **326**, 96–192 (2011).

[43] M. E. J. Newman, *Networks: an introduction* (Oxford University Press Oxford; New York, 2010).

[44] M. Van Raamsdonk, *New Frontiers in Fields and Strings: TASI 2015 Proceedings of the 2015 Theoretical Advanced Study Institute in Elementary Particle Physics* (World Scientific , 2017), pp. 297–351.

[45] L. Freidel, R. G. Leigh, and D. Minic, International Journal of Modern Physics D **23**, 1442006 (2014).

[46] D.-W. Chiou, International Journal of Modern Physics D **24**, 1530005 (2014).

[47] G. Bianconi and C. Rahmede, Scientific reports **5**, 1 (2015).

[48] Z. Wu, G. Menichetti, C. Rahmede, and G. Bianconi, Scientific reports **5**, 1 (2015).

[49] R. Bousso, Reviews of Modern Physics **74**, 825–874 (2002).

[50] J. Maldacena, International Journal of Theoretical Physics **38**, 1113–1133 (1999).

[51] L. Susskind, Fortschritte der Physik **64**, 551–564 (2016).

[52] S. Nezami *et al.*, arXiv preprint arXiv:2102.01064 (2021).

[53] S. W. Hawking, arXiv preprint arXiv:1509.01147 (2015).

[54] N. Bao, S. M. Carroll, and A. Singh, International Journal of Modern Physics D **26**, 1743013 (2017).

[55] M. B. Hastings, Journal of Statistical Mechanics: Theory and Experiment **2007**, P08024–P08024 (2007).

[56] R. Cuzinatto, C. de Melo, and C. N. de Souza, arXiv preprint arXiv:1904.01966 (2019).

[57] H. R. Grimsley, S. E. Economou, E. Barnes, and N. J. Mayhall, Nature Communications **10**, (2019).